

**UNIVERSITY OF CENTRAL OKLAHOMA**  
Edmond, Oklahoma  
College of Graduate Studies and Research

**MONITORING TEMPERATURE DISTRIBUTION DURING LASER-TISSUE  
INTERACTION FOR CANCER TREATMENT USING MAGNETIC  
RESONANCE THERMOMETRY**

**A THESIS**

**SUBMITTED TO THE GRADUATE COLLEGE**

In the fulfillment of the requirements

for the degree of

**MASTER OF SCIENCE IN ENGINEERING PHYSICS**

By

**Akhee Sarker**

Edmond, Oklahoma

2009

**MONITORING TEMPERATURE DISTRIBUTION DURING LASER-TISSUE  
INTERACTION FOR CANCER TREATMENT USING MAGNETIC  
RESONANCE THERMOMETRY**

**A THESIS**

**APPROVED FOR THE DEPARTMENT OF ENGINEERING AND PHYSICS**

**08/03/2009**



By \_\_\_\_\_  
Committee Chairperson



\_\_\_\_\_  
Committee Member



\_\_\_\_\_  
Committee Member

## **ACKNOWLEDGEMENTS**

I would like to extend my sincere gratitude to my thesis advisor, Dr. Wei R. Chen, for his support and excellent guidance to pursue the project successfully. I consider myself very fortunate to have had the opportunity to work on this project with him. I would like to thank IDeA Network of Biomedical Research Excellence (INBRE) for funding this project. I would also like to thank my project collaborator, Kelvin Le, for his sincere help to conduct the experiments. I would also like to thank the rest of my supervising committee, Dr. Weldon Wilson and Dr. Jaehoon Seong. In addition, I want to thank my parents who were always there with love and encouragement. Finally, I would like to thank my husband, Okhil Kumar Nag for his constant encouragement and emotional support during my pursuit of my Master's Degree.

## TABLE OF CONTENT

|   |          |
|---|----------|
| Acknowledgments   | iii      |
| Table of Contents   | iv       |
| List of Figures   | vi       |
| Abstract  | 1        |
| <br>  |          |
| <b>SECTION 1. INTRODUCTION</b>  | <b>3</b> |
| <br>  |          |
| <b>SECTION 2. THEORY OF MAGNETIC RESONANCE</b>                            | <b>6</b> |
| <b>THERMOMETRY AND THERMAL TISSUE INTERACTIONS</b>                        |          |
| 2.1 Principles of MRT   | 6        |
| 2.2 Magnetic Resonance Imaging (MRI) Using Phase Difference               | 7        |
| 2.3 Magnetic Resonance Thermometry Parameters                             | 14       |
| 2.3.1 PRF shift-based method for MRT                                      | 14       |
| 2.3.2 The Diffusion Coefficient (D)                                       | 16       |
| 2.3.3 $T_1$ , $T_2$ and $T_2^*$ Relaxation                                | 17       |
| 2.3.4 TE, TR and $\theta$   | 19       |
| 2.3.5 Spatial Resolution  | 20       |
| 2.4 Temperature Distribution, Heat -Tissue Interaction and Selectivity in | 20       |
| 2.4.1 Responses of Normal Tissue to Temperature Increase                  | 21       |
| 2.4.2 Responses of Tumor Tissue to Temperature Increase                   | 21       |
| 2.4.3 Selectivity of Photothermal Interaction using Light Absorbing       | 22       |

|  |           |
|--|-----------|
| Chromophore  |           |
| 2.4.4 Heat Induced Immune Response against Tumor Tissue  | 23        |
| <b>SECTION 3. EXPERIMENT SET UP AND METHODS</b>  | <b>24</b> |
| 3.1 Introduction   | 24        |
| 3.2 Laser  | 24        |
| 3.3 Power Meter  | 25        |
| 3.4 7.1 Tesla MRI System, Optical Fiber and Plastic Chamber  | 26        |
| 3.5 Phantom Gel  | 27        |
| 3.6 Indocyanine Green (ICG) Dye Ball and IGC Solution  | 27        |
| 3.7 Temperature Measurement of Embedded Indocyanine Dye Ball into<br>Phantom and Chicken Breast tissue | 29        |
| 3.8 Gel Phantom and Ex Vivo Chicken Breast Tissue Temperature Distribution<br>Monitoring               | 31        |
| <b>SECTION 4. RESULTS</b>  | <b>33</b> |
| <b>SECTION 5. DISCUSSIONS AND SUMMARY</b>  | <b>51</b> |
| <b>REFERENCES</b>  | <b>55</b> |
| <b>APPENDIX: TEMPERATURE CALIBRATION ALGORITHM USING<br/>MATHEMATICA 5.2</b>                           | <b>66</b> |

## LIST OF FIGURES & TABLES

|                     |   |    |
|---------------------|---|----|
| <b>Figure 2.1.</b>  | Phase mapping pulse sequence  | 13 |
| <b>Figure 2.2.</b>  | Illustration of phase difference in MRT   | 15 |
| <b>Figure 3.1.</b>  | Diomed 805 nm Laser   | 25 |
| <b>Figure 3.2.</b>  | Power meter and related devices   | 25 |
| <b>Figure 3.3.</b>  | 7.1 Tesla Superconductor small animal MRI system  | 26 |
| <b>Figure 3.4.</b>  | Optical Fiber   | 26 |
| <b>Figure 3.5.</b>  | Plastic Chamber in which the chicken breast tissue and Phantom gel were secured inside MRI system.    | 27 |
| <b>Figure 3.6.</b>  | 3D view of Phantom Gel Cylinder by the MRI system   | 28 |
| <b>Figure 3.7.</b>  | Molecular structure of indocyanine green (ICG).   | 28 |
| <b>Figure 3.8.</b>  | Schematic of Dye Ball inside Phantom Gel  | 29 |
| <b>Figure 3.9.</b>  | 3D Cross sectional view of Dye ball embedded beneath a thin layer of chicken breast using MRI.        | 30 |
| <b>Figure 3.10.</b> | Chicken breast with ICG of concentration 0.08% under irradiation of laser power of $2 \text{ W/cm}^2$ | 31 |
| <b>Figure 4.1.</b>  | Calibration using optical sensor (OS) and MRI for 2 averages  | 34 |
| <b>Figure 4.2.</b>  | Temperature change profile of chicken breast tissue   | 35 |
| <b>Figure 4.3.</b>  | Calibration experiments using optical sensor (OS) and MRI for 1 average                               | 36 |
| <b>Figure 4.4.</b>  | Temperature change profile of chicken breast tissue with susceptibility artifacts                     | 37 |

|                     |  |    |
|---------------------|--|----|
| <b>Figure 4.5.</b>  | Temperature difference ( $\Delta T$ ) versus cycles plot to show the early divergence.   | 38 |
| <b>Figure 4.6.</b>  | Temperature calibration of MRT using optical sensor. This plot shows the temperature inaccuracy between the MRT and optical sensor | 38 |
| <b>Figure 4.7.</b>  | Temperature profile for falsified temperature reading  | 39 |
| <b>Figure 4.8.</b>  | Temperature profile of point divergence: a sudden drop in temperature  | 39 |
| <b>Figure 4.9.</b>  | Temperature calibration using water Tube for 1 average with TE=3.312 ms, TR = 200 ms, 25.6s/cycle and IT = 4.1 °C                  | 40 |
| <b>Figure 4.10.</b> | Temperature calibration profile mapping for a water tube   | 41 |
| <b>Figure 4.11.</b> | Temperature calibration using water tube for 1 average with TE = 2.91 ms, TR = 200 ms, 25.6 s/cycle and IT = 2.66 °C               | 41 |
| <b>Figure 4.12.</b> | Temperature calibration profile map for a water tube showing shading artifact  | 42 |
| <b>Figure 4.13.</b> | Temperature calibration of MRI using optical sensor for 1 average with TE = 4.296 ms TR = 200 ms 25.6 s/cycle IT = 3.56 °C         | 42 |
| <b>Figure 4.14.</b> | Temperature calibration profile map for chicken breast tissue with longer TE.  | 43 |
| <b>Figure 4.15.</b> | Graphical representations of susceptibility artifact effect  | 43 |
| <b>Figure 4.16.</b> | Temperature profile in two different points in a chicken breast sample   | 44 |

|                     |   |    |
|---------------------|---|----|
| <b>Figure 4.17.</b> | Susceptibility artifact and geometry selection  | 45 |
| <b>Figure 4.18.</b> | A temperature map profile in the latter stages of calibration                                       | 45 |
| <b>Figure 4.19.</b> | Temperature mapping of a 0.056% ICG concentrated dye ball embedded within the chicken breast tissue | 46 |
| <b>Figure 4.20.</b> | Temperature mapping of a 0.08% ICG concentrated chicken breast tissue                               | 47 |
| <b>Figure 4.21.</b> | Temperature profiles using MRT and thermocouple under the same parameters                           | 48 |
| <b>Figure 4.22.</b> | Chicken breast tissue temperature mapping versus time with 0.056% ICG concentration                 | 49 |
| <b>Figure 4.23.</b> | Chicken breast tissue temperature mapping versus time with 0.08 % ICG concentration                 | 49 |
| <b>Figure 4.24.</b> | A chicken tissue temperature mapping versus time with 0.1 % ICG concentration                       | 49 |
| <b>Table 2.1.</b>   | Comparison between low resolution and high resolution MRI   | 20 |
| <b>Table 2.2.</b>   | Effects of increase temperature in living tissue.   | 22 |
| <b>Table 3.1.</b>   | Testing Parameters  | 32 |



## ABSTRACT

One of the major challenges in the field of cancer treatment is to induce a prolonged systemic immune response. Laser immunotherapy has shown its potential as a minimally invasive alternative for many cancer patients due to its ability to target and destroy cancerous cells while leaving minimal damage to surrounding tissue. Temperature distribution is a crucial factor during laser-tissue interaction in the treatment of tumors. In order to optimize laser immunotherapy, it is important to monitor the temperature distribution in target tissue during laser irradiation. Among the currently available temperature measurement techniques, Magnetic Resonance Thermometry (MRT) is the only feasible method for non-invasive, real-time, three-dimensional temperature mapping. In this study, we investigated the temperature distribution in gel phantom during laser irradiation using MRT. Spherical gel phantoms, as targets containing a light-absorbing agent, indocyanine green (ICG), of different concentrations were embedded inside normal phantom gels or in chicken breast tissue and were irradiated by an 805 nm diode laser. A 7.1 Tesla magnetic resonance imaging (MRI) system and a specially designed algorithm were used for *ex vivo* temperature mappings. The MRI signals were recorded using a fast low-angle shot (FLASH) sequence during laser irradiation with different values of MRI parameters such as TE (echo time), TR (repetition time), and NEX (number of excitation). The relative position of the proton, as determined by its phase, was obtained from the MRI signal. The phase data were reconstructed to obtain temperature distributions. Temperature elevation of target gels containing 0.056% ICG irradiated with laser of 2.0 watt/cm<sup>2</sup> power density showed better selectivity compared to

that of 0.08% and 0.10% ICG. However, phantom gels in chicken breast tissue with 0.08% ICG treated with laser of 1.0 watt/cm<sup>2</sup> power density showed a considerable temperature elevation in the range of 10-35°C. Our results suggest that the effectiveness of the photothermal treatment depends on various parameters such as laser power, dye concentration, time of laser irradiation, and time of relaxation. This study provided important information for optimizing laser immunotherapy.

**Key Words:** Cancer treatment, laser immunotherapy, magnetic resonance thermometry (MRT), magnetic resonance imaging (MRI), indocyanine green (ICG), gel phantoms, fast low-angle shot (FLASH), TE (echo time), TR (repetition time), NEX (number of excitation), temperature mapping.

## SECTION 1. INTRODUCTION

One of the many challenges facing modern medicine is the ability to diagnose and treat metastatic cancers. Some of the most common options for patients, who are diagnosed with metastatic cancer, are chemotherapy, radiation, and surgery [1-3]. However, patients are well aware of the dire consequences of these drastic measures. For many years, standard cancer therapies have been sought to target a specific malignant cell, but with only limited success [4-7]. Unfortunately, these successes have also been accompanied by varying degrees of toxicity, and there is currently no standard therapy that can eradicate clinical disease and prevent recurrence while leaving normal tissue unharmed. In fact, the treatment of primary tumors using local interventions, such as surgery and radiation, may stimulate the growth of metastases at remote sites [8-10]. Recently, several approaches to optimize the tumor-specific immunity hold promise for effective treatment and lasting cure [11-13]. These approaches are based on the exceptional specificity to the immune system, through different interventions and use the host immune responses to fight against their own tumors. Among these methods, one particularly approach, laser immunotherapy, shows great promise [14-18]. It has shown its potential as a non-invasive alternative due to its ability of target specificity and destruction of cancerous cells while leaving minimal damage to surrounding tissues [19].

Photothermal reaction produces hyperthermia and coagulation of tissue; it can be an effective means in tumor tissue destruction due to the sensitivity of tumor cell to temperature elevation [20-23]. The selective, local photothermal ablation technique, using a combination of a laser and a light absorbing chromophore, exploits the nature of

cancer cells: their vulnerability to temperature elevation compared to healthy cells [24-25]. However, the laser immunotherapy is not only desired for its selective therapeutic nature, but also, for its long-term systemic immunological response it induces using active immunological stimulation [26-28]. With the knowledge of how cancer cells respond to temperature, one can optimize the treatment parameters, such as power density, time, and chemical dosage. The best way to optimize the selective photothermal effect is through real-time, three-dimensional observation of temperature distribution in target and surrounding tissues during the laser irradiation. Currently, the only non-invasive method to achieve such observation is through Magnetic Resonance Thermometry (MRT) [29-31].

Photothermal interaction is a crucial component of laser immunotherapy. It has shown to be effective in cancer treatment when the temperature of the tissue is raised above the cell damage threshold [32]. Temperature distribution is an important factor during laser-tissue interaction in the treatment of tumors. Monitoring the temperature distribution *in vivo* using MRT can lead to optimization of laser immunotherapy. By choosing appropriate pulse sequence, MRT can provide 3D temperature mapping noninvasively during the photothermal treatment, providing useful information for laser light delivery [33]. MRT can also be used to detect zones of different thermal damage in target and surrounding normal tissues [34, 35].

In this study, we investigated temperature distributions in gel phantom and in chicken breast tissue with different configurations of light absorption enhancement with ICG of different concentrations during laser irradiation using MRT. MRT is the only available method for a non-invasive, three-dimensional temperature mapping, using the

temperature dependency of the proton chemical shift [36]. The target spherical gel phantoms containing light absorbing-agent, indocyanine green (ICG), were embedded inside normal phantom gels and chicken breast tissue. ICG was also injected directly to the chicken breast tissue to increase selective photon absorption. All the thermal experiments were carried out with an 805-nm Diomed laser of different settings. Using a 7.1 Tesla MRI system and a specially designed algorithm, *ex vivo* temperature mappings were obtained.

In the following sections, basic concept of MRT, experimental set ups, and MRT data collections and analysis are presented, discussed, and concluded by summary and conclusions.

## SECTION 2. THEORY OF MAGNETIC RESONANCE THERMOMETRY AND THERMAL TISSUE INTERACTIONS

### 2.1 Principles of MRT

Living tissues are mainly composed of water molecules, each of which contains two hydrogens. When a powerful magnetic field of the MRI scanner is applied to the living tissue, the protons of these hydrogens align with the direction of the field. A second radio frequency (RF) electromagnetic field is then briefly turned on, causing the protons to absorb some of its energy. When this field is turned off the protons release this energy at a radio frequency, which can be detected by the MRI scanner. The position of protons in the body can be determined by applying additional magnetic fields during the scan, which allows an image of the body to be constructed. Diseased tissue, such as tumors, can be detected because the protons in different tissues return to their equilibrium state at different rates.

There are several temperature-sensitive Nuclear Magnetic Resonance (NMR) properties that could be used for MRT, such as the relaxation time, diffusion coefficient of water, and the proton resonance frequency (PRF). The PRF shift method possesses many attributes that make it suitable for high-temperature thermal therapies, including good temperature sensitivity, linearity and reversibility with temperature, and ease of measurement and interpretation. The time a proton takes to decay into their initial position can be manipulated by an outside heat source, such as a laser beam by the following equation [33, 37-39]

$$\Delta T = \frac{\Delta\Phi}{\gamma B_0 \alpha TE}, \quad (1)$$

where  $\Delta T$  is the change in temperature,  $\Delta\Phi$  is the change in phase,  $\gamma$  [rad/T] is the gyromagnetic ratio,  $B_0$  is the MRI magnetic field which is independent of temperature,  $\alpha$  is the temperature-dependent water chemical shift in ppm/ $^{\circ}\text{C}$ , which is constant within measurement range, and TE is the time of echo formation of the field echo pulse sequences. The phase  $\Phi$  is the relative position of the proton which can be calculated from the imaginary and real data of MRI signal. The change of the phase can be determined by [37, 38]

$$\Delta\Phi_n = \text{ArcTan}\left(\frac{\text{Re}_n \text{Im}_o - \text{Re}_o \text{Im}_n}{\text{Re}_o \text{Re}_n + \text{Im}_o \text{Im}_n}\right), \quad (2)$$

where Re and Im represent the real and imaginary components of the complex MRI signals.

Phase change can be induced by an external force, such as laser irradiation. Therefore, we can correlate the external intervention with the phase change, and hence with temperature change. The signal in an MR image can be computed from a complex number,  $z = re^{i\Phi}$ , where  $r$  is the signal strength and  $\Phi$  is the phase. We can also present signals using real component  $a = r \cos\Phi$  and the imaginary component  $b = r \sin\Phi$ . Among other factors the phase depends on the temperature, and thus this can be used for obtaining temperature mapping.

## 2.2 Magnetic Resonance Imaging (MRI) Using Phase Difference

MRI is one of the best methods for non-invasive, real-time, three dimensional temperature mapping and target visualization [33]. The water proton resonance frequency (PRF) shift is the most promising method for thermometry with high spatial and temporal data acquisition. In the PRF method, effects on the local magnetic field

shielding caused by the electron clouds around the proton due to temperature changes can be monitored. The resonance frequency of a proton at a certain temperature is determined by the strength of the magnetic flux density,  $B_0$ , of an external field and the shielding effect, caused by the currents induced in the electron cloud in the direction to cancel the external field. When temperature rises, the motion of water molecules intensifies, distorting, extending, and/or breaking hydrogen bonds of the molecules; thus, an electron cloud at higher temperatures is freer from the restraint of the electrical bonding force than at lower temperatures. The attenuation of hydrogen bonding induces more current in the electron cloud, strengthening the shielding effect. As a result, the resonance frequency of the water proton becomes lower. This frequency change with temperature can be normalized in the form of a chemical shift or thermal shift [39]. The temperature coefficient of the proton chemical shift of pure water has been previously determined as 0.01 ppm /°C [39].

With temperature increase, the screening effect of bounded electrons of the proton is increased, which weakens the local magnetic field of the proton further and shows the negative shift of water PRF. The PRF method was first investigated by Hindman *et al* [40]. The magnetic field experienced by a proton within tissue,  $B_{local}$ , has the following relationship [41] with the principle external magnetic field  $B_0$ ,

$$B_{local} = [1 - \sigma(T)]B_0, \quad (3)$$

where  $\sigma(T)$ , the chemical shift, is the screening factor and  $B_0$  is the MRI magnetic field which is independent of temperature. The relationship between temperature and the water proton chemical shift can be obtained. When there is a non-aqueous, temperature-insensitive compound in the region under observation, it can be used as an internal



reference for measuring water proton resonance frequency. The temperature-dependent chemical shift can be defined as [41, 42]

$$\delta_{W-R}[ppm] = \frac{\omega_W(T) - \omega_R(T)}{\omega_R(T)} \cdot 10^6 \quad (4)$$

$$\approx \frac{\omega_W(T) - \omega_R(T)}{\omega_{RF}(T)} \cdot 10^6 \approx (-\sigma_W(T) + \sigma_R + \chi_W(T) - \chi_R(T)) \cdot 10^6, \quad (5)$$

where

$$\begin{aligned} \omega_W(T) &= \gamma B_0 (1 - \sigma_W(T) + \chi_W(T)) \\ \omega_R(T) &= \gamma B_0 (1 - \sigma_R(T) + \chi_R(T)) \end{aligned} \quad (6)$$

where  $\omega_W(T)$  [rad/sec] and  $\omega_R(T)$  [rad/sec] are the resonance frequencies of water and the reference compound at a certain temperature,  $T$ , respectively,  $\omega_{RF}$  [rad/sec] is the central RF frequency of the transceiver/receiver,  $\gamma$  [rad/T] is the gyromagnetic ratio,  $\chi(T)$  is the magnetic susceptibility of tissue, and  $\sigma_W(T)$  and  $\sigma_R(T)$  are the shielding constants for water and the reference, respectively, denoting the degree of magnetic shielding effect of the electron cloud.

The relationship between temperature and the chemical shift is denoted as [42]

$$T = \frac{\sigma_{W-R}}{\alpha} + \beta, \quad (7)$$

where  $\alpha$  [ppm/ $^{\circ}$ C] is the hypothetical temperature co-efficient and temperature offset at which the chemical shift becomes zero is  $\beta$  [ $^{\circ}$ C]. From the relationship among the temperature, the temperature-dependent chemical shift, and the shielding constants, the temperature difference,  $\Delta T$  [ $^{\circ}$ C], can be denoted by the equation [34]

$$\Delta T = \frac{\Delta \delta_{W-R}}{\alpha} \quad (8)$$

$$\approx \frac{\omega_W(T) - \omega_R(T)}{\alpha \omega_{RF}(T)} \cdot 10^6 \approx \frac{\Delta\omega}{\alpha\omega} \cdot 10^6.$$

The quantitative relationship becomes, with Larmor frequency,  $\omega = \gamma B_{local}$ ,

$$\Delta\omega / \Delta T = \alpha\gamma B_{local} \text{ and } \Delta\omega = \alpha\gamma B_{local} \Delta T, \quad (9)$$

where  $B_{local} = B_0(1 - \sigma(T))$  and  $\omega(T) = \gamma B_0(1 - \sigma(T))$ . After proton spin magnetizations are flipped down, they will rotate in the transverse plane at Larmor frequencies proportional to the local magnetic fields which vary due to temperature differences. The phase difference, due to temperature dependent frequency shift, will build up as time goes by. For a spin-echo signal, the magnetization is in the transverse plane before and after the refocusing pulse [37]. A crusher gradient is a correction gradient that preserves the desired signal pathways while eliminating the unwanted ones by manipulating the phase of the signals. A crusher gradient typically consists of two lobes with the same polarity, one immediately before a refocusing RF pulse and the other immediately after. These two gradient lobes form a crusher pair [37]. Thus the applied phases are:

$$\Phi_W = \int_0^\tau \omega_W dt \quad (10)$$

$$\Phi_R = \int_0^\tau \omega_R dt. \quad (11)$$

Because the refocusing RF pulse negates the phase, the net accumulation after the crusher pairs is given by

$$\Phi_R - \Phi_W = \Delta\Phi = \omega\Delta t = \gamma B_0 \Delta t. \quad (12)$$

Here the time interval is equivalent to the time of echo formation TE of the field echo pulse sequences. Then equation (12) becomes

$$\Delta\Phi = \omega\Delta t = \gamma B_0 TE . \quad (13)$$

The water proton chemical shift change can be calculated from a region of interest in the center of the phase difference images at the time of echo formation, TE, using the following relationship [43],

$$\Delta\delta_{W-R} = \frac{\Delta\Phi \times 10^6}{\gamma B_0 \cdot TE} . \quad (14)$$

Comparing the equations (8) and (14), it is observed that the phase difference,  $\Delta\Phi$ , is linearly related to the temperature difference,  $\Delta T$ , which can be expressed as the following equation,

$$\Delta\Phi = \alpha\gamma B_0 \cdot TE\Delta T , \quad (15)$$

where the  $\gamma$  is the gyro-magnetic ratio of hydrogen ( $\gamma = 2\pi \cdot 42.57$  MHz/T) and TE is the echo time of gradient echo pulse sequence. The chemical shift field is the sum of the temperature-independent contribution, such as  $B_0$  field in homogenous tissue and a temperature dependent contribution [33],

$$\sigma(T) = \sigma_0 + \sigma_T(T) , \quad (16)$$

where  $\sigma_0$  is a temperature-independent factor and  $\sigma_T(T)$  is linearly related to the temperature. At a relative small temperature range,  $\sigma_T(T)$  can be considered linearly dependent on temperature  $T_0$ [33],

$$\sigma(T) = \sigma_0 + \alpha T , \quad (17)$$

where  $\alpha$  is the temperature-dependent water chemical shift in ppm/ $^{\circ}$ C, which is constant within the measurement range. From the relationship of phase difference and temperature difference in equation (15), it can be inferred that the temperature change is proportional to the phase change of image at each corresponding pixel. The fluctuation

of the external magnetic field can cause a phase change in the MRI thermal measurement. It is generally assumed that the water proton chemical shift to lower frequencies, with a higher temperature, is caused by rupturing, stretching, or a small amount of bending of the hydrogen bonds. Thus, this means a reduction in the average degree of association of the water molecules, and these shifts are evidence of an increased shielding constant of the protons. The change of proton chemical shift with temperature is thought to be caused by the observed variations of the magnetic field inhomogeneity. In fact, the local magnetic field inhomogeneity,  $\Delta B_0$ , can be represented as the sum of the field inhomogeneity,  $\delta B_0$ , and the chemical shift field caused by magnetic shielding effect,  $B_{local}$ , which depends on the temperature distribution  $T(\mathfrak{R})$  [44],

$$\Delta B_0(T(\mathfrak{R})) = \delta B_0(\mathfrak{R}) + B_{local}(T(\mathfrak{R})), \quad (18)$$

in which  $\mathfrak{R}$  represents a spatial vector. The inhomogeneity of the magnet and the magnetic susceptibility of the sample produce  $\delta B_0$ . However, it must be canceled out to measure the variations of the change of the chemical shift field,  $\Delta B_{local}$ , with temperature only, for which it is assumed that  $\delta B_0$  does not change with temperature for diamagnetic materials. These variations can be calculated by subtracting the field distribution,  $\Delta B_0(T_0(\mathfrak{R}))$ , at a reference temperature,  $T_0$ , from the field distribution  $\Delta B_0(T(\mathfrak{R}))$  after a change in temperature. We obtain, then, the field distribution difference as a function of the temperature distribution  $\Delta T(\mathfrak{R})$ ,

$$\begin{aligned} \Delta B_{local}(\Delta T(\mathfrak{R})) &= B_{local}(T(\mathfrak{R})) - B_{local}(T_0(\mathfrak{R})) \\ &= \Delta B_0(T(\mathfrak{R})) - \Delta B_0(T_0(\mathfrak{R})). \end{aligned} \quad (19)$$

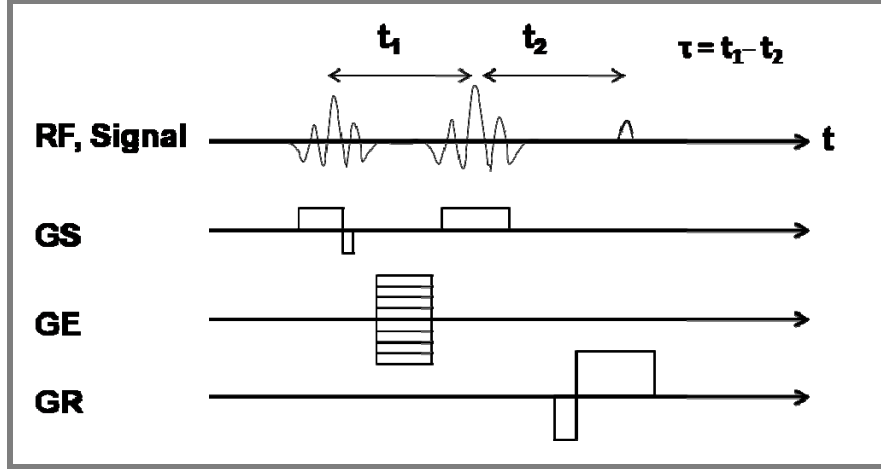


Figure 2.1 Phase mapping pulse sequence.

Such field inhomogeneities can be calculated from the phase image  $\Phi(T(\mathfrak{R}))$  obtained with the phase mapping method using pulse sequence, as shown in Figure 2.1. The time difference,  $\tau$ , between relaxation time  $t_1$  and relaxation time  $t_2$ , is related to the phase,

$$\Phi(T(\mathfrak{R})) = \gamma \Delta B_0(T(\mathfrak{R})) \tau, \quad (20)$$

where  $\gamma$  is the gyromagnetic ratio. The temperature distribution can then be calculated using the following equations that subtract the phase distribution at a reference temperature from that after a change in temperature,

$$\Delta T(\mathfrak{R}) = [T(\mathfrak{R}) - T_0(\mathfrak{R})], \quad (21)$$

$$\Delta T(\mathfrak{R}) = \Delta B_{local}(\Delta T(\mathfrak{R})) / \alpha B_0, \quad (22)$$

$$\Delta T(\mathfrak{R}) = \Delta \Phi(T(\mathfrak{R})) / \alpha \gamma \tau B_0, \quad (23)$$

$$\Delta T(\mathfrak{R}) = [\Phi(T(\mathfrak{R})) - \Phi(T_0(\mathfrak{R}))] / \alpha \gamma \tau B_0. \quad (24)$$

The temporal resolution obtained with a field echo pulse sequence is superior to that obtained with a spin echo pulse sequence. In this case,  $\tau$  is equivalent to the echo time, TE, of the field echo pulse sequences. Then equation (24) becomes

$$\Delta T(\mathfrak{R}) = [\Phi(T(\mathfrak{R})) - \Phi(T_0(\mathfrak{R}))] / \alpha\gamma TEB_0. \quad (25)$$

The phase change corresponding to magnetic field change from equation (22), (23), and (25) is

$$\Delta\Phi = TE\gamma\Delta B. \quad (26)$$

This corresponds to the temperature change,  $\Delta T$ ,

$$TE\gamma\Delta B = \alpha\gamma B_0 \cdot TE\Delta T. \quad (27)$$

Therefore,

$$\Delta B = B_0\alpha\Delta T, \quad (28)$$

and

$$\Delta T = \frac{\Delta B}{B_0\alpha} = \frac{\Delta\Phi}{\alpha\gamma TEB_0}. \quad (29)$$

As will be seen, high temperature sensitivity is required for the MRI thermometry; therefore, phase difference PRF shift MR thermometry was chosen for this study.

### 2.3 Magnetic Resonance Thermometry Parameters

In order to improve the temperature sensitivity during the energy storage period, phase image was used. The temperature sensitivity for the phase image is proportional to  $1/\text{SNR}$  (signal-to-noise ratio), which in turn is related to TE (echo time), TR (repetition time), flip angle  $\theta$ , spatial resolution, and temporal resolution.

#### 2.3.1 PRF shift-based method for MRT

In Nuclear Magnetic Resonance (NMR), the Proton Resonance Frequency (PRF) is given by  $\omega = \gamma B_0$ . However, the exact value of  $\gamma$  for water protons is influenced by the

electronic configuration of the water molecule, giving rise to a chemical shift, which is temperature dependent. It is believed that temperature-induced alterations in hydrogen bonding that electronically screen the external magnetic field from the protons would lead to a shift in the PRF, which is proportional to the local magnetic field. It has been shown that the temperature-dependent chemical shift constant,  $\alpha$ , of water protons, over temperature ranges of interest to thermal therapy, is  $-0.01 \text{ ppm}/^\circ\text{C}$  [39]. With the exception of fat, all types of soft tissue have been found to behave in a similar way [45]. MRI thermometry methods can be implemented based on this frequency shift. The first approach directly measures the absolute frequency shift, which is called chemical shift imaging or spectroscopic imaging. However, due to  $T_2$  relaxation, one can only have a limited time window to observe the temporal signal.

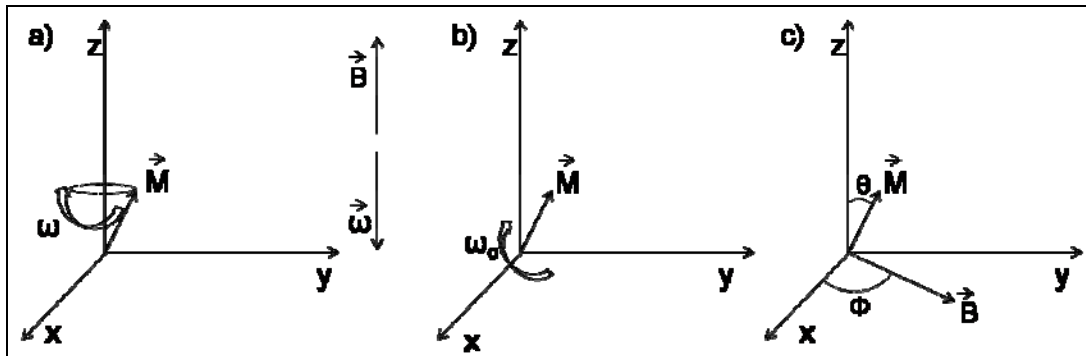


**Figure 2.2.** Illustration of phase difference in MRT. a) and b) spin magnetizations are flipped into the transverse plane from the z-axis ( $B_0$  direction), and c) phase  $\Phi$  accumulates with time.

The other approach is a phase difference method which is illustrated in Figure 2.1 and 2.2. At the time of echo formation,  $TE$ , phase difference is (see section 2.2),

$$\Delta\Phi = TE\gamma B_0\alpha\Delta T. \quad (30)$$

By optimizing imaging parameters, detection of temperature changes within 1°C has been demonstrated by several groups [15]. Based on this idea, other modified sequences, such as echo-shifted Turbo FLASH (Fast Low Angle Shot) [46], Hybrid EPI (Echo Planar Imaging) [47], have been investigated for pseudo real-time clinical situations. In spite of hardware instability problems reported [45], this method remains the most sensitive approach. In addition, the PRF of soft tissues has been found to behave similarly to that of water except for fat. In contrast, the temperature coefficients of the other parameters, such as relaxation time and diffusion coefficients are strongly tissue-dependent. The water proton chemical shift allows measurement of absolute temperature using an appropriate internal reference.

### 2.3.2 The Diffusion Coefficient (D)

The thermal Brownian motion of an ensemble of molecules is described by the diffusion constant  $D$ . The relationship between temperature and the diffusion constant is exponential [48],

$$D \approx e^{-E_a(D)/\kappa T} \quad (31)$$

where  $E_a(D)$  is the activation energy of the molecular diffusion of water,  $k$  is the Boltzmann constant, and  $T$  is absolute temperature. The dependence of  $D$  on temperature can be described as [48]

$$\frac{dD}{DdT} = \frac{E_a(D)}{\kappa T^2}. \quad (32)$$

Compared with  $T_1$ , the activation energy for diffusion of water is substantially higher, about 0.2 eV, and the temperature dependency of changes in  $D$  amounts to about 2 %/°C. MRI based on  $D$  method has good sensitivity [49, 50]. However, there are several



practical problems associated with the feasibility of the D based MRI method. These are related to the mobility of water molecules, which depend on barriers such as the cellular structures, proteins constitution, and membranes thickness in the tissue. The two major consequences for MRI based on D are nonlinear dependence of D on temperature and direction dependence mobility of water in the tissue. The first one is due to temperature dependent permeability of the barriers and the second one is due to the anisotropic nature of the barriers. Any coagulation processes lead to large changes in the diffusion constant since diffusion pathways are modified. Nonlethal physiological effects can also lead to large changes in D [51].

### **2.3.3 $T_1$ , $T_2$ and $T_2^*$ Relaxation**

In NMR, a strong magnetic field is used to partially polarize the nuclear spins. Taking protons as the most common example, the excess of proton spin in the direction of the magnetic field constitutes a small net magnetization of the material. To set up the conditions for the observation of an NMR signal, strong radio frequency radiation is applied to the sample at the appropriate frequency to produce "spin flips". From the quantum point of view, the RF photons are absorbed by some of the protons to flip them from parallel to the magnetic field to anti-parallel, a higher energy state. When the exciting RF field is switched off, the protons tend to return to their lower energy state. This "relaxation" back to a state where their spins are parallel to the static magnetic field produces a small amount of RF radiation, which is detected as the NMR signal. Ultimately, the two different time constants for decay are typically observed.

The longer of the two time constants is usually labeled  $T_1$  and is associated with the decay of the field component that is parallel to the applied static magnetic field  $B_0$ . This field direction is usually taken to define the z-axis of the system. This time constant is sometimes called the longitudinal time constant. In addition, it is also called the spin-lattice relaxation time. Since the magnetic potential energy is proportional to the projection along this axis, a change in the magnetization along this axis involves the exchange of energy, which implies that the spin has interacted with its environment.

For applications of magnetic resonance imaging of the body, the interaction is important, because it implies the capacity in differentiating between different types of tissue. The shorter of the two time constants is usually labeled  $T_2$ , and is associated with the decay of the field component that is perpendicular or transverse to the applied static magnetic field,  $B_0$ . The relaxation time,  $T_2$ , is the time required for the transverse component of  $\mathbf{M}$  to decay 37% of its initial value via irreversible processes. This time constant is sometimes called the spin-spin relaxation time or the transverse relaxation time constant.  $T_2$  relaxation in gradient echo sequence is called  $T_2^*$  relaxation and the relation can be shown as,

$$\frac{1}{T_2^*} = \frac{1}{T_2} + \frac{1}{T_{2M}} + \frac{1}{T_{2MS}} \quad (33)$$

where  $T_{2M}$  is the dephasing time due to the main field inhomogeneity and  $T_{2MS}$  is the dephasing time due to the magnetic susceptibility. The relaxation time,  $T_1$ , is the time required for the z component of  $\mathbf{M}$  to return to 63% of its original value following an excitation pulse. Thus,  $\mathbf{M}_0$  is parallel to  $\mathbf{B}_0$  at equilibrium and that energy absorption will rotate  $\mathbf{M}_0$  into the transverse plane.  $T_1$  relaxation provides the mechanism by which the

protons give up their energy to their original orientation. These time constants also vary with the tissue type [52, 53].

### 2.3.4 TE, TR and $\theta$

The Signal to Noise Ratio (SNR) in the phase difference images are both proportional to TE, which scales phase difference and  $e^{-TE/T_2}$ , which corresponds to signal decay [37, 48-49, 54]. Thus,

$$SNR \propto TE \cdot e^{-TE/T_2^*} . \quad (34)$$

The maximization of the above expression would lead to the choice of TE,

$$TE = T_2^* . \quad (35)$$

The steady-state saturation-recovery MR signal can be expressed as follows,

$$Signal \propto \frac{1 - e^{-TR/T_1} \sin \theta}{1 - e^{-TR/T_1} \cos \theta} \quad (36)$$

where  $\theta$  is the flip angle. Maximization of the angle would lead to the so-called Ernest angle  $\theta^E = \cos^{-1}(e^{-TR/T_1})$  and can be expressed as follows,

$$\theta^E = \sqrt{(1 - e^{-TR/T_1})(1 + e^{-TR/T_1})} . \quad (37)$$

From this expression, the longer TR is the better, since magnetizations are better recovered with longer TR. However, with longer TR, the fewer averages are possible. If one assumes that the number of averages during a fixed time window is inversely proportional to TR, then the resultant SNR will be proportional to  $1/\sqrt{TR}$ .

Thus, the overall SNR at Ernest angle can be expressed as

$$SNR \propto \frac{1}{\sqrt{TR}} \cdot \frac{1 - \exp(-TR/T1)}{1 + \exp(-TR/T1)}. \quad (38)$$

### 2.3.5 Spatial Resolution

Table 2.1 shows the comparison between low resolution and high resolution MR images. In addition, intra-voxel cancelling can happen with reduced resolution in several scenarios. Firstly, main magnetic field ( $B_0$ ) inhomogeneities can cause signal cancelling over a big voxel. Secondly, if temperature changes inside a large voxel are too big, phase aliasing can occur in the voxel, leading to erroneous temperature conversion. Thirdly, averaging a voxel results in the angles of integrated magnetization vectors, which is not equivalent to the average phase angles of all magnetizations [37, 48, 49].

**Table 2.1:** Comparison between low resolution and high resolution MRI

|                        | <b>Low Resolution</b> | <b>High Resolution</b> |
|------------------------|-----------------------|------------------------|
| SNR                    | High                  | Low                    |
| Imaging Time           | Short                 | Long                   |
| Size of Matrix         | Smaller               | Bigger                 |
| Sampling Error         | High                  | Low                    |
| Intra-voxel Cancelling | More problematic      | Less problematic       |

## 2.4 Temperature Distribution, Heat -Tissue Interaction and Selectivity in MRT

Heat transfer in the tissue during laser irradiation affects the temperature distribution and tissue responses in the target tissue and surrounding tissue. Due to the relatively

large physical dimensions and inhomogeneous characteristics of biological tissues, the diffusion process needs to be modeled during laser irradiation. Using the absorbed energy in tissue as the heat source, the thermal energy diffusion process can be determined; hence, providing information on thermal responses of tissue. Several factors make predicting the heating distribution difficult. Because energy deposition at the target depends on the tissue's ability to absorb the applied energy, is a function of tissue composition. The tissue parameters can change as the tissue undergoes changes during thermal treatment, for example, when proteins coagulate. In addition, heat conduction through perfusion and diffusion can vary with tissue architecture, tissue composition, and physiological parameters. Therefore, the role of MRI is to visualize and quantify the deposition of heat energy in the treated and surrounding tissue with adequate spatial and temporal resolution. Consequently, the success of MR image guided thermal therapy depends on the accuracy with which temperature can be estimated.

#### **2.4.1 Responses of Normal Tissue to Temperature Increase**

Living tissue is very sensitive to temperature increase. Table 2.2 shows the effects of temperature increase in tissue.

#### **2.4.2 Responses of Tumor Tissue to Temperature Increase**

Heat has a strong cytotoxic effect in tumor tissue than in normal tissue as thermal effects are more profound in the acidic (low pH) conditions present in poorly oxygenated tumors and observed cytotoxicity associated with temperature increase [61]. However, heat alone has only a limited effect in cancer treatment; in the early whole-body

hyperthermia treatment, only a small portion of complete responses and short response duration were observed [62-68]. Furthermore, when conventional hyperthermia is used in cancer treatment, damage to surrounding normal tissue is often unavoidable. The thermal effect can be strongly augmented when combined with a novel treatment modality using a near-infrared laser, a laser absorbing dye, and an immunoadjuvant [63-67].

**Table 2.2** Effects of increase temperature in living tissue.

| <b>Temp (°C )</b> | <b>Effects on living tissue*</b>   |
|-------------------|--|
| 40                | Blood flow increase in both tumor and normal tissue [55, 56]                           |
| 41.5              | Cytotoxicity occurs in tumor cell [57]   |
| 42.5              | Vascular destruction in tumor tissue [58]  |
| >43               | Rate of “Cell kill” double for every 1°C increment above 43°C [59, 60]                 |
| <43               | Rate of “Cell kill” decrease by a factor 4 to 6 for every 1°C drop below 43°C [59, 60] |

\*It has been found that tumor tissue is more sensitive to temperature increase than the normal tissue. [25]

### **2.4.3 Selectivity of Photothermal Interaction using Light Absorbing Chromophore**

Use of *in situ* light absorbing chromophore facilitates the absorption of light in the selected region of the target tissue. The chromophore absorbs light to reach an excited high-energy state. When the chromophore returns to the ground state, it heats up the surrounding tissue by releasing the absorbed energy. As a result, temperature of the target tissue increases steadily. The concentration of the chromophore and the power of

the laser need to be optimized to achieve desirable temperature elevation in the target tissue, resulting in selective photothermal tissue destruction.

Chen, *et al*, proposed the use of light-absorbing chromophore and near-infrared laser to induced selective photothermal laser-tissue interaction [69]. Specifically, an 805-nm diode laser and indocyanine green (ICG) were first used for thermal treatment of rat tumors, both in vitro and in vivo [70-72].

#### **2.4.4 Heat Induced Immune Response against Tumor Tissue**

Different levels of heating can bring different immunomodulatory effect on the target tissue [73]. Temperature between 39-40°C influences the activities of immune cells, such as antigen presenting cells (APC), T cells, and natural killing cells (NK cell). Temperatures between the ranges of 41–43°C can increase the immunogenicity of tumor cells. Temperatures above 43°C produce antigen source for induction of an anti-tumor immune response [26]. These antigens include tumor-associated antigens, thermally induced heat shock proteins and a large amount of self-antigens. Combination of thermally induced antigen and traditional tumor vaccine can boost immunological memory and amplify immune response.

## SECTION 3. EXPERIMENT SET UPS AND METHODS

### 3.1 Introduction

In this study, all the experiments were conducted using an 805 nm Diomed laser. A power meter was used to measure the laser output. Phantom gel and dye balls were made carefully for desired concentrations. Dye balls were embedded inside the phantom gel and chicken breast tissue to simulate tumors buried inside normal tissue. The cylindrical shape phantom gel and chicken breast tissue were placed into a 7.1 Tesla Bruker 730 USR 30 cm horizontal-bore superconducting small animal MRI system in a plastic chamber. Laser was delivered to the target region through an optical fiber with microlens. The fiber contains a 400- $\mu\text{m}$  core, with an output spot of 57 mm diameter at 100 mm with half-angle divergence of 15.9 degrees. Chemical shift based on water proton density resonance frequency was used for temperature mapping as discussed in Section 2. The studies were conducted at the University of Central Oklahoma and at the Oklahoma Medical Research Foundation (OMRF). The transformation from complex data to a temperature map is computed through a specially developed algorithm using *Mathematica 5.2<sup>TM</sup>*.

### 3.2 Laser

An 805 nm Diomed laser, shown in Figure 3.1, with a maximum power output of 25 watts, was used to deliver the photothermal treatment to the target tissue in the experiment. The laser beam was directed to the treatment site into the MRI machine



through an optical fiber with a diffusion lens (Pioneer Optics, Windsor Locks, CT) to ensure even distribution of laser energy on the treatment surface.



**Figure 3.1.** Diomed 805 nm Laser.

### 3.3 Power Meter

Figure 3.2 displays a power meter used to measure the power delivered by the 805 nm Diomed laser to ensure the actual power received by the treatment surface.



**Figure 3.2** Power meter and related devices.

### 3.4. A 7.1 Tesla MRI System, Optical Fiber and Plastic Chamber

Figure 3.3 shows the MRI system used for the experiments. Optical fiber with microlens is shown in Figure 3.4. The fiber was kept at a certain distance from the irradiated surface so that a desired beam size could be achieved. A plastic chamber shown in Figure 3.5 was used to secure the chicken breast tissue, gel phantom, and water inside the MRI chamber.



**Figure 3.3.** 7.1 Tesla Superconductor small animal MRI system.

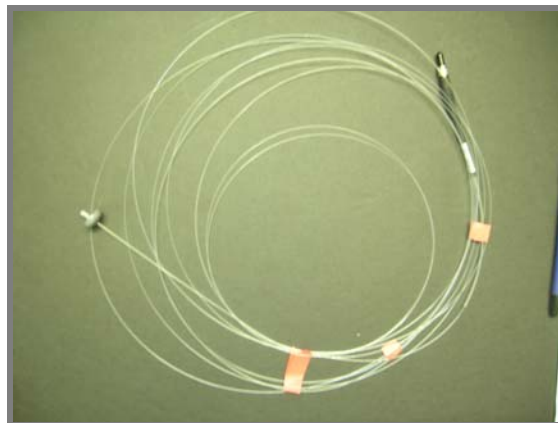


**Figure 3.4.** Optical fiber.

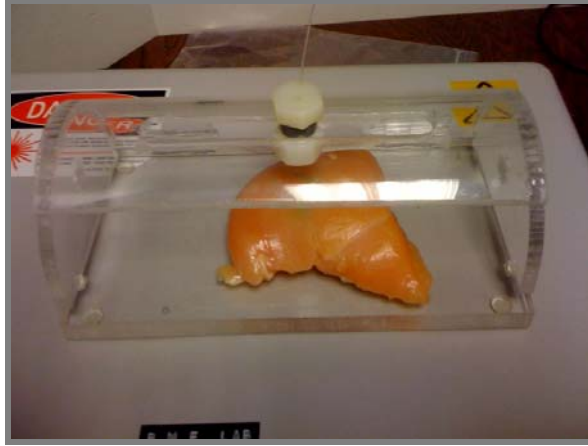


**Figure 3.5.** Plastic Chamber in which the chicken breast tissue and Phantom gel were secured inside MRI system.

### **3.5 Phantom Gel**

In order to stimulate thermal and optical properties of mammary tissue, phantom gel was made by mixing 4% of Gelatin, 20% of lyposin (10% fat), and 76% of water. All the ingredients were mixed and placed on a hot plate. When the gelatin had completely dissolved, it was removed from the hot plate and allowed to cool. The solution was solidified and stored in the refrigerator. A cylinder of phantom gel was used to stimulate biological tissue of certain configuration. Figure 3.6 shows the 3D view of phantom gel inside the MRI chamber.

### **3.6 Indocyanine Green (ICG) Dye Ball and ICG Solution**

Indocyanine Green, a water-soluble chromophore, was used as a laser-absorbing agent because its absorption band ( $\sim 790$  nm) almost perfectly matches with the 805-nm laser and makes the selective photothermal reaction possible. The molecular structure of

ICG is given in Figure 3.7. ICG has been used in both diagnostic and treatment purpose [74-80].

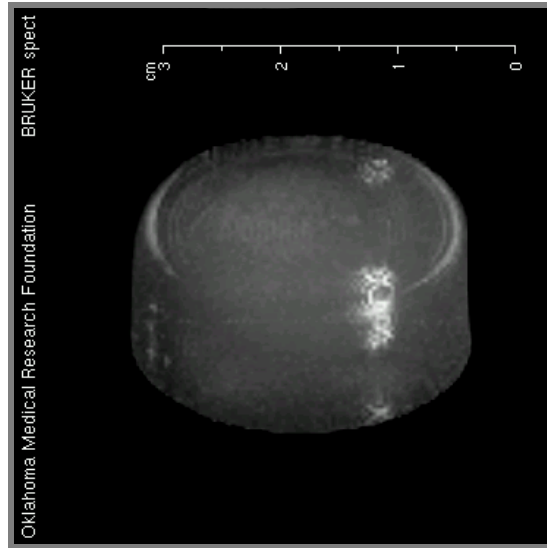


**Figure 3.6.** 3D view of Phantom Gel Cylinder by the MRI system.

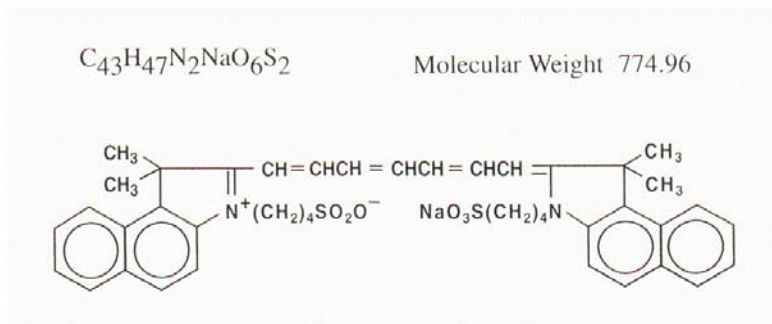


**Figure 3.7.** Molecular structure of indocyanine green (ICG).

To make an ICG solution of concentration  $X$  (g/mL), with mass of dry ICG  $Y$ (g), volume  $V$ (mL), we used the formula:  $V=Y/X$ . An initial ICG solution was made with a higher concentration. The initial ICG solution was made from raw ICG powder with an

appropriate volume of aqueous solvent. The dye balls with desired concentrations were made from the ICG solution of a higher concentration.

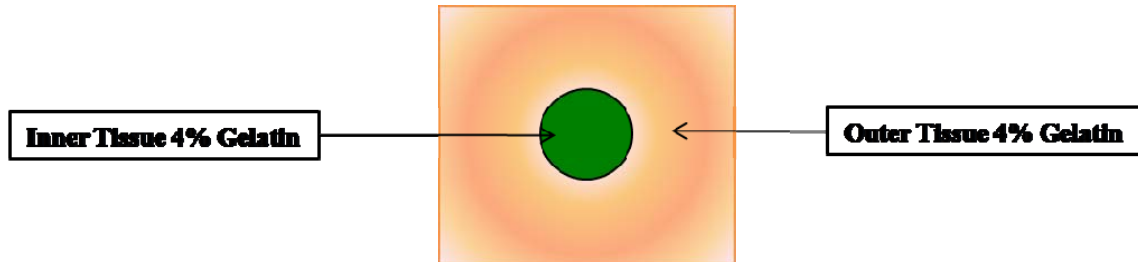


Figure 3.8. Schematic of Dye Ball inside Phantom Gel.

### 3.7 Temperature Measurement of Embedded Indocyanine Dye Ball into Phantom Gel and Chicken Breast Tissue

The MRT method relies on the relationship between the phase change of water proton and the temperature dependent chemical shift to deduce the temperature change [20-23, 81-84]. From the complex phase data, one can extract its components (real and imaginary). Using the real and imaginary part of the collected data, the phase difference can be calculated using equation 2. The phase is a property of a real signal related to the temporal and/or spatial wavelength and influences the signal only in the range of the principal values, i.e. those lying in the range of  $(-\pi, \pi)$ . Sensors and basic signal processing produce a wrapped phase. This wrapping is a nonlinear process producing an output lying in the principal range of  $(-\pi, \pi)$ . To be able to generate an image, this wrapped output phase needs to be unwrapped. The associated issue with the phase, ranging from  $-\pi$  to  $\pi$ , has a phase unwrapping problem. In the absence of noise, this unwrapping can be performed optimally by summing the wrapped phase differences [85].

However, for the purpose of this experiment, the temperature elevation is lower than the threshold range for a phase wrap to occur. In addition, to reduce any ambiguity, the initial temperature of the samples was the room temperature.

A phantom gel dye ball was embedded the middle of phantom gel and chicken breast tissue. The dye ball was selected instead of ICG injection, because injection of dye solution into chicken tissue leads to a non-uniform distribution of dye with variable concentrations throughout its volume of diffusion. Figures 3.9 and 3.10 show the 3D cross sectional and real view of the dye ball embedded chicken breast, respectively. The optical fiber was placed directly over the center of the phantom gel dye ball, embedded within the chicken breast tissue. The beam radius was calculated for different concentrations. The chicken breast tissue was allowed to reach room temperature, and then placed inside the MRI chamber where the laser beam was placed through an optical fiber.

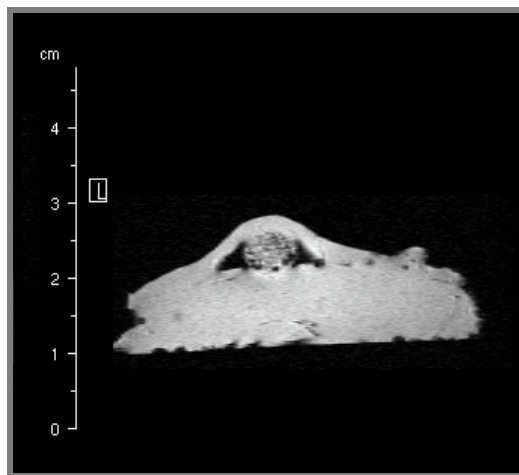


**Figure 3.9.** 3D Cross sectional view of dye ball embedded beneath a thin layer of chicken breast using MRI.

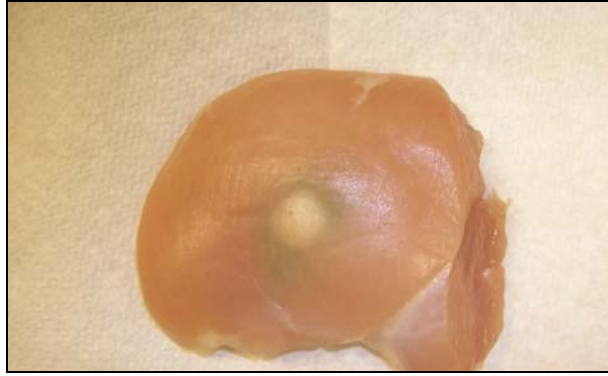


**Figure 3.10.** Chicken breast with ICG of concentration 0.08% under irradiation of laser power of 2 W/cm<sup>2</sup>.

### **3.8 Gel Phantom and *Ex Vivo* Chicken Breast Tissue Temperature Distribution Monitoring**

The study of temperature distribution was conducted using 10% fat based gel models (76% water, 20% liposyn, and 4% gelatin) and chicken breasts with embedded dye balls. A total of six phantom gel and twelve chicken breast samples were tested. Numerous parameters, such as power density, tissue type, and chemical concentrations were tested for the best outcomes. The laser beam diameter was adjusted to obtain a power density of 1.0 W/cm<sup>2</sup>, 1.5 W/cm<sup>2</sup>, 2.0 W/cm<sup>2</sup>, and 2.5 W/cm<sup>2</sup>, respectively. The MRI signal was recorded using a fast low-angle shot (FLASH) sequence during the laser irradiation process. A single session consisted of a 5 min testing period, a 10 min of laser irradiation, and a 15.4 min of relaxation with a total of 24 phase changes. Each phase represented a time interval of 76 sec. The thermal map dimensions were 128 by 128 pixels. The phase information, corresponding to the temperature changes, is related to the reference point. Table 3.1 displays the parameters used for the experiments.

**Table 3.1** Testing Parameters

| <b>Power Density<br/>(Watt/cm<sup>2</sup>)</b> | <b>Concentration of ICG in<br/>phantom gel</b> |      |      | <b>Concentration of ICG in chicken<br/>breast tissue</b> |      |      |
|--|--|------|------|--|------|------|
| 1.0  | 0.056  | 0.08 | 0.10 | 0.056  | 0.08 | 0.10 |
| 1.5  | 0.056  | 0.08 | 0.10 | 0.056  | 0.08 | 0.10 |
| 2.0  | *N/A   | *N/A | *N/A | 0.056  | 0.08 | 0.10 |
| 2.5  | *N/A   | *N/A | *N/A | 0.056  | 0.08 | 0.10 |

\*Due to low melting point of phantom gel, these parameters were excluded.



## SECTION 4. RESULTS

The MRI data was obtained using FLASH MRI sequence. The real and imaginary data were collected and reconstructed from raw MRI data by MR image processing. The gradient echo MRI data were acquired during the experiments. The real and imaginary data were used to extract the phase information using arctangent of the ratio of imaginary and real parts of MRI data as shown in equation 2 in Section 2. The algorithm was implemented in *Mathematica 5.2<sup>TM</sup>*. The phase differences were calculated by subtracting the reference phase image, pixel-by-pixel, from all of the subsequent phase images acquired during the experiments. The magnitude signal of a certain image was used as a filter with a certain threshold set in the algorithm to eliminate the noise points outside the target gel region. The temperature change was obtained from the phase information. The MRI parameters such as TE, TR, and flip angle were optimized to have high signal noise ratio, low phase noise, and short data acquisition time. The temperature information was exported to an Excel file for pixel-to-pixel analyses and comparison. By locating the target region, we can plot temperature versus time to determine the highest increase of temperature. At time  $t$ , when laser irradiation ended; the temperature is the highest, as determined by exporting the matrix to the Excel sheet. The thermal images were represented using a color-coded lookup table scheme to show the temperature of each pixel.

In order to determine the system factor, a series of calibration tests were performed using different materials. It is inferred from the data that there exist a sampling threshold for every TE chosen. Figure 4.1 shows a temperature calibration between the optical

sensor (OS) and the MRT for 2 averages. This was a test for divergence in the system, with duration of 1.5 hours. In this figure, TE is 3.935 ms, TR is 200 ms, and initial temperature (IT) is 3.2 °C. The experiment observation was conducted and recorded as 51.2 s/cycles.

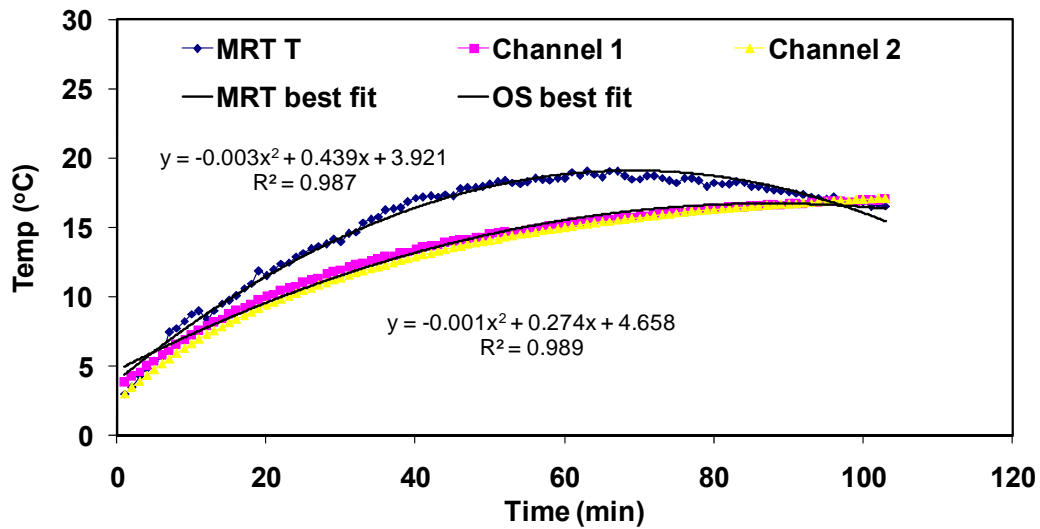
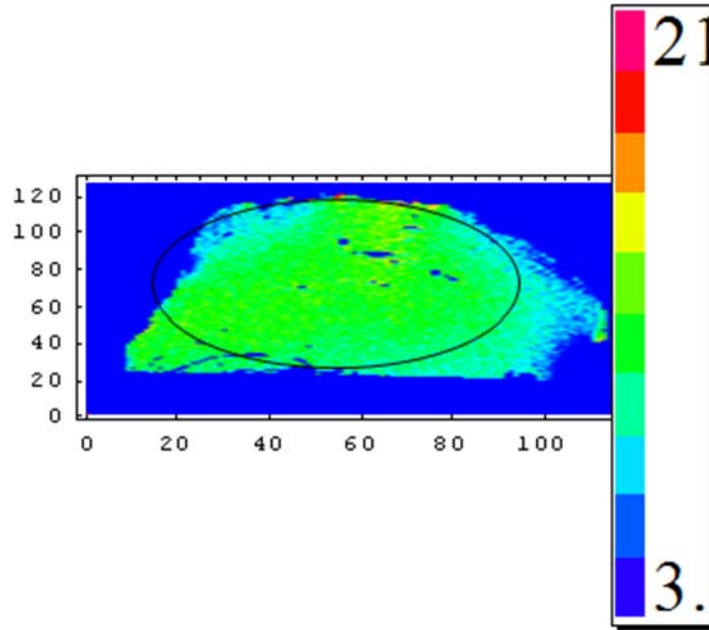


Figure 4.1. Calibration using optical sensor (OS) and MRI for 2 averages.

Temperature change profile of chicken breast tissue is shown in Figure 4.2. In this scan, the number of excitation (NEX) or average was 2. The result shows an influx in artifact (the circled region), and the correct color representation is in the blue (the peripheral region). The graph (Figure 4.1) shows this correlation is higher than the usual increase in temperature. The two average parameters were temporary abandoned in the next scans due to the artifact. The bar shows a total temperature change over a 30 min period. The dimensions of the figure are 128 x 128 x 20 x 105.



**Figure 4.2.** Temperature change profile of chicken breast tissue.

Figure 4.3 shows another temperature calibration experiment between the optical sensor (OS) and the MRT for 1 average. The test was for 1.0 hour. In this figure TE is 3.935 ms, TR is 200 ms, and initial temperature (IT) is 4.8 °C. The experiment observation was conducted and recorded as 25.6 s/cycles. There was a 5 sec interval before every new scan. In this case, the time of delay is 12 cycles, and the total time delay is 5 min and 7 seconds. As one can see, there are three segments. The ideal time of delay is close to zero. However, the minimum time is restricted to the system since it takes about 5 sec to prepare before every new scan. The circled region in Figure 4.4 shows the magnetic susceptibility artifact due to the air pocket. The dimensions of the figure are 128 x 128 x 5x155 and the slice of interest was the thirteenth slice. In theory, if the system is defaulted before the time of divergence, we can continue to scan the sample. The time and rate of divergence is also tissue specific (i.e. water or chicken

breast). We compensated it by working in segments of 15-20 min scans and allowed the system to rest or default for a brief one-second delay (assuming there existed minor physical changes during that time). It was hypothesized that the time of divergence was a function of TE. There was a low SNR due to poor pre-scan adjustment and caused a susceptibility artifact. We set the scan to have four 20 cycles' series with a one-second delay. However, this was a compromise for the divergence issue we had with the long scans. Although artifacts are present, a good temperature image can be obtained, as we know from Curie's Law susceptibility effect, which decreases with increasing temperature.

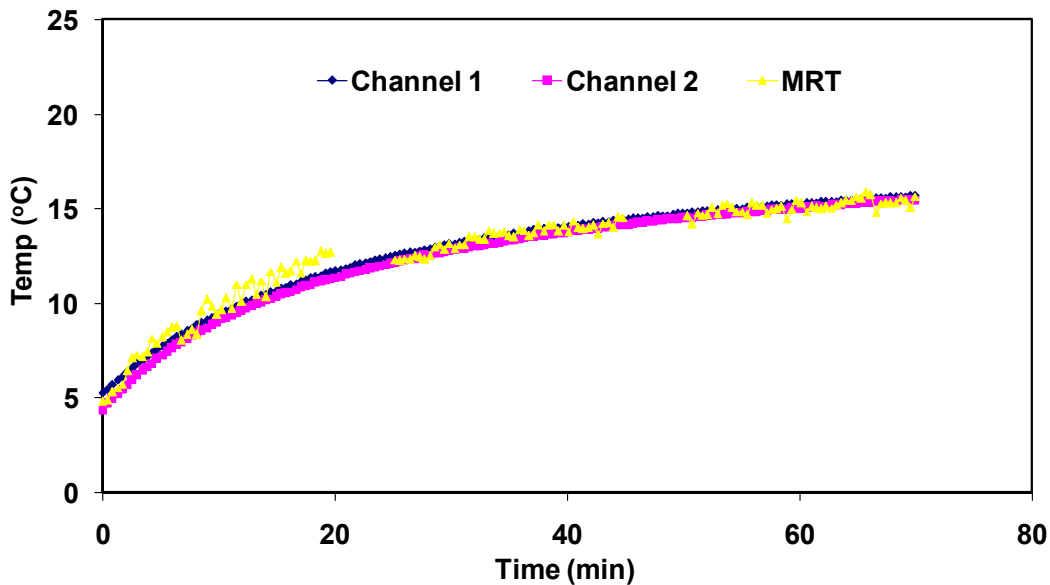


**Figure 4.3.** Calibration experiments using optical sensor (OS) and MRI for 1 average.

When we paid close attention to the second portion, after the divergence artifact and the calibration of the profile, we surprisingly obtained a precise temperature reading. It was the change that mattered the most in the MRT scan, and in this case the change in

temperature held in the latter portion. Figure 4.5 and Figure 4.6 show the early divergence and sudden drop of temperature during the MRI scan. This also shows the inaccuracy between the Thermo-couple and the MRI.

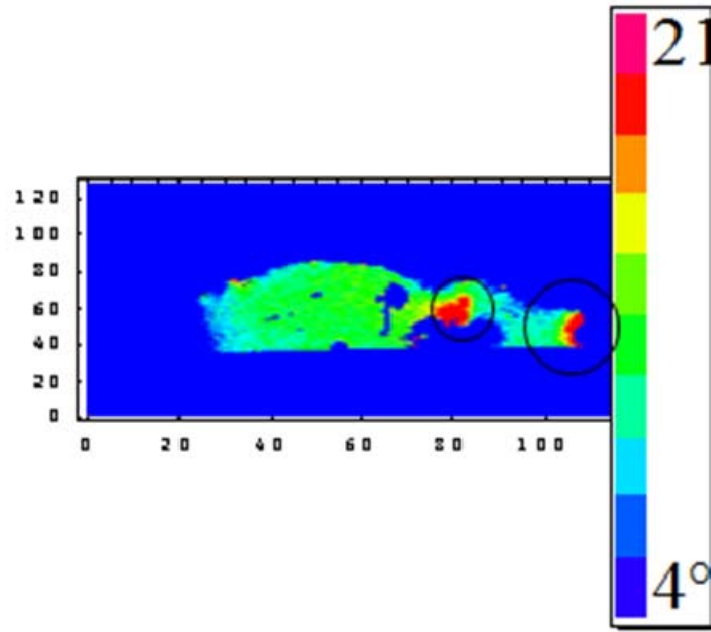


**Figure 4.4.** Temperature change profile of chicken breast tissue with susceptibility artifacts.

Figures 4.7 and 4.8 show the Mathematica temperature profile of an inaccurate temperature reading and a sudden drop of temperature. The temperature point of interest was taken at (80, 60) in the x and y coordinate. The circled region represents the inaccurate temperature reading from the scan (the subtle color difference).

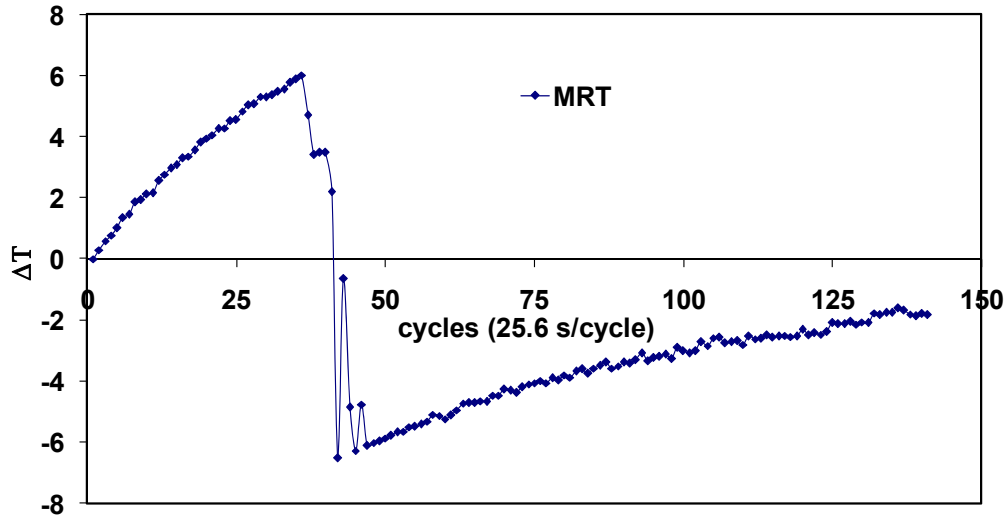


**Figure 4.5.** Temperature difference ( $\Delta T$ ) versus cycles plot to show the early divergence.

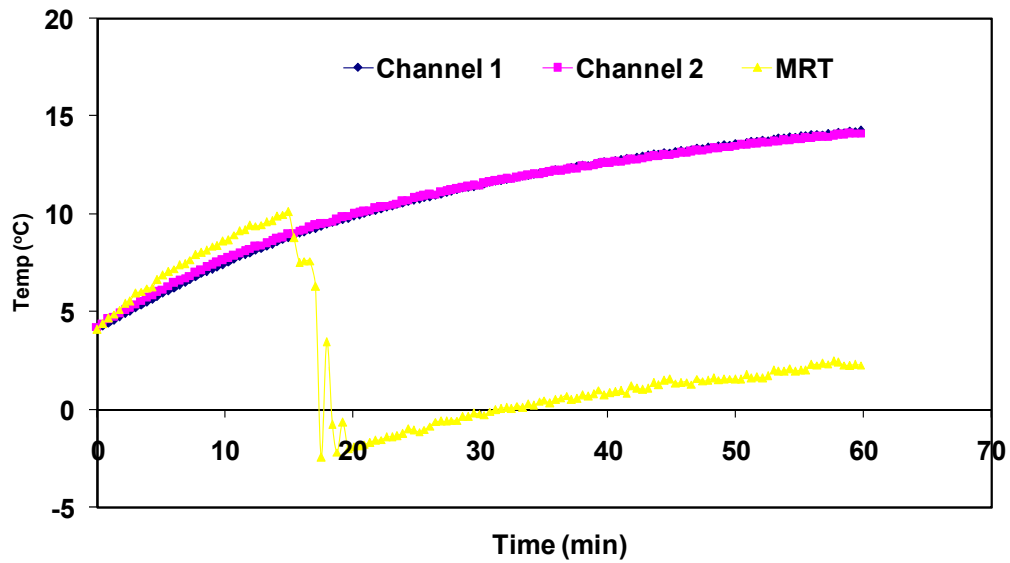


**Figure 4.6.** Temperature calibration of MRT using optical sensor. This plot shows the temperature inaccuracy between the MRT and the optical sensor.

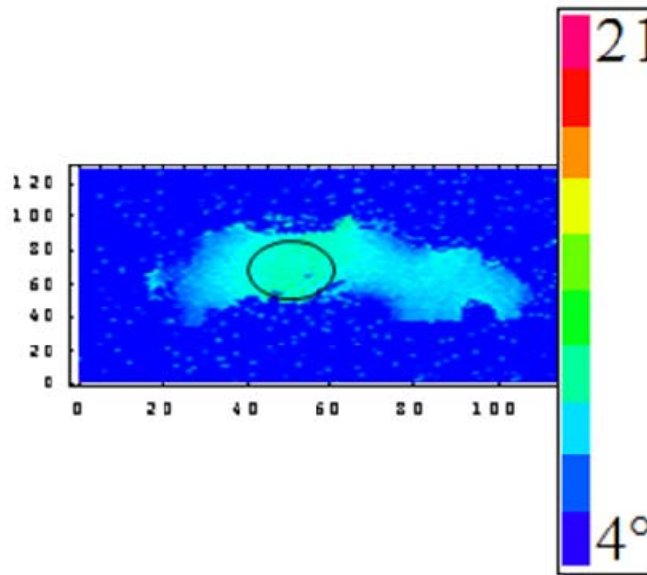


**Figure 4.7.** Temperature profile for falsified temperature reading.

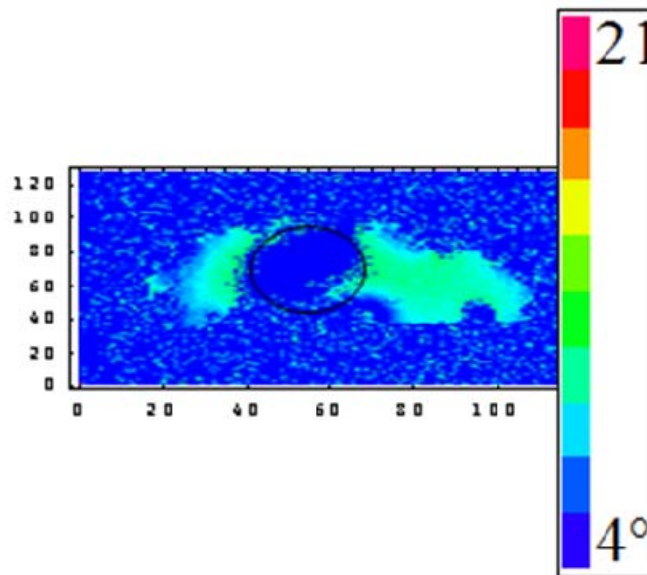


**Figure 4.8.** Temperature profile of point divergence: a sudden drop in temperature.

A shorter TE was tested for SNR. The temperature calibration is shown in Figure 4.9 and the temperature profile is shown in Figure 4.10. It is well that shorter TE results in a longer scan time before divergence. However, the time was not too different from 3.935

ms. In addition, the temperature map shows a homogenous signal. Also, the rate of divergence differed from past scans, which was promising. The dimensions are 128 x 128 x 5 x 211 and the slice of interest was the third slice. The result shows a similar time of divergence to that of chicken breast (around 25 min).

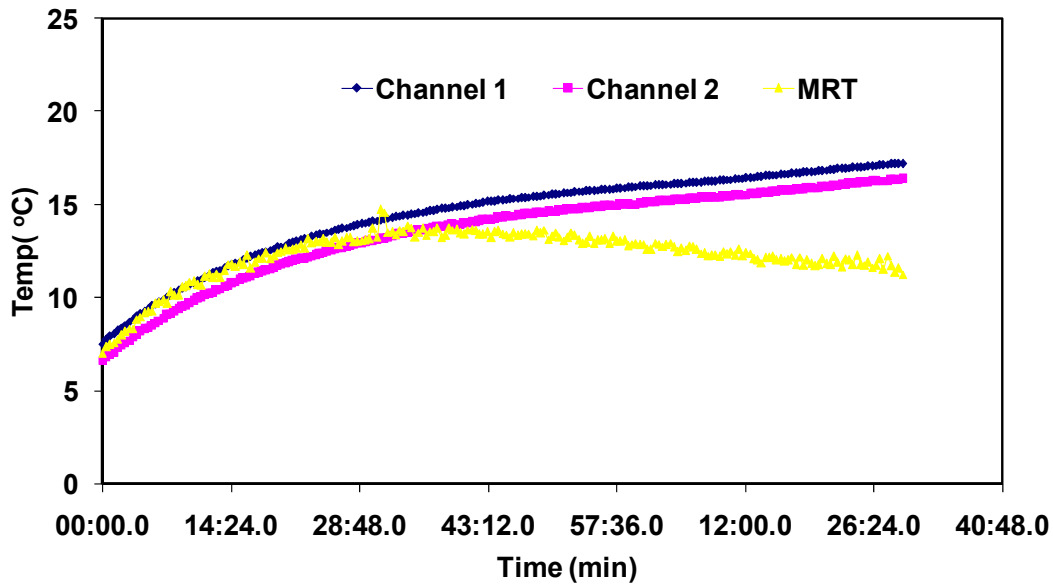


**Figure 4.9.** Temperature calibration using water tube for 1 average with TE=3.312 ms, TR = 200 ms, 25.6 s/cycle, and IT = 4.1 °C.

The temperature reading deviated significantly inside the circled area and right on target outside for the experiment (Figure 4.11 and Figure 4.12). The dimensions are 128 x 128 x 5 x 141 and the Slice of Interest is the 3<sup>rd</sup> slice again. We implemented the hypothesis of shorter TE equals longer scan time without systemic divergence. However, we arrived with a new daunting artifact: the susceptibility artifact. It was not conspicuous until this particular scan that we were convince of the susceptibility artifact. If we could only get rid of the susceptibility artifact, the shorter TE seemed to be a



leading candidate for longer scans. The graph in Figure 4.11 shows that the shorter TE equals the longer scan time without systematic divergence.

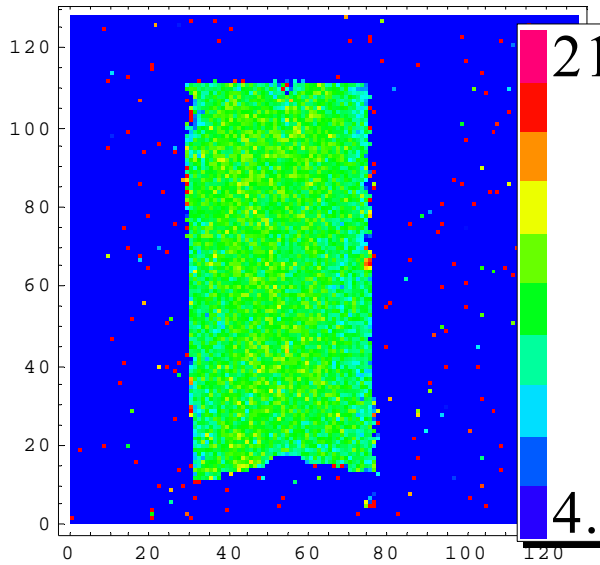


**Figure 4.10.** Temperature calibration profile mapping for a water tube.

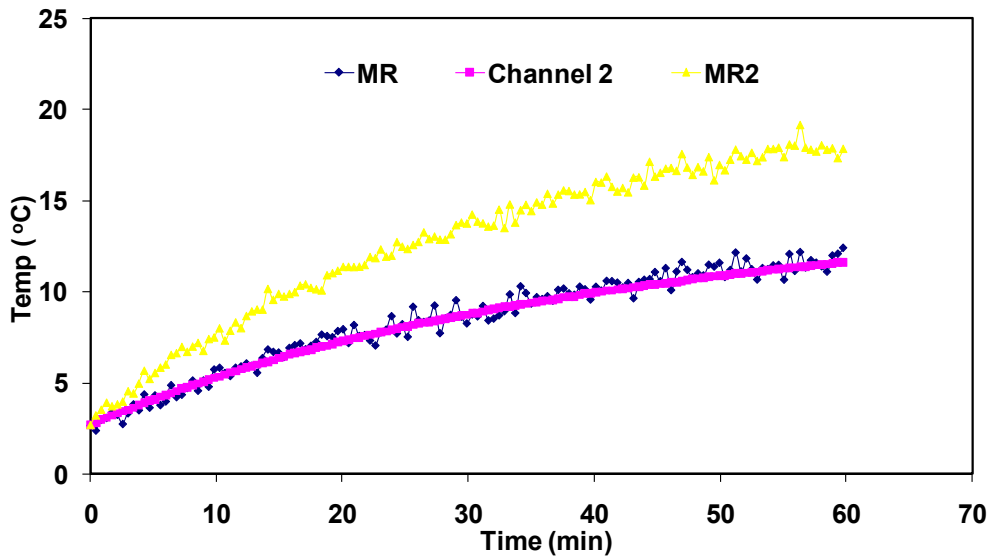


**Figure 4.11.** Temperature calibration using water tube for 1 average with TE = 2.91 ms, TR = 200 ms, 25.6 s/cycle, and IT = 2.66 °C.

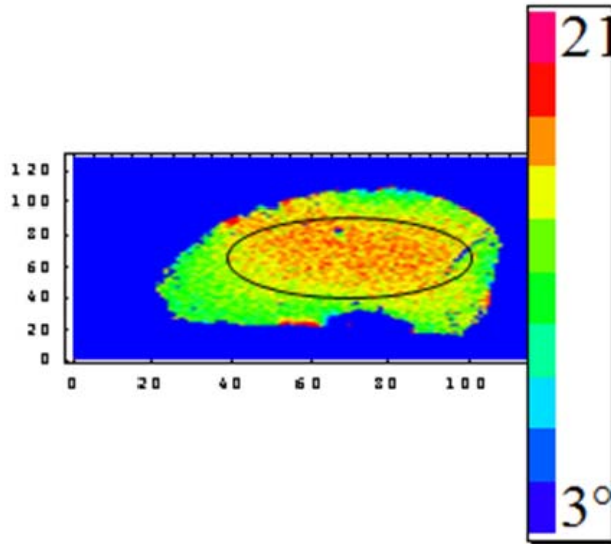


**Figure 4.12.** Temperature calibration profile map for a water tube showing susceptibility artifact.

The Hermits RF pulse sequence was used for the scan show in Figure 4.13 and Figure 4.14. The result then can be compared to other pulse sequences. Magnetic susceptibility was seen. At 4.296 ms, the result was decent. Dimensions: 128 x 128 x 5 x 35.

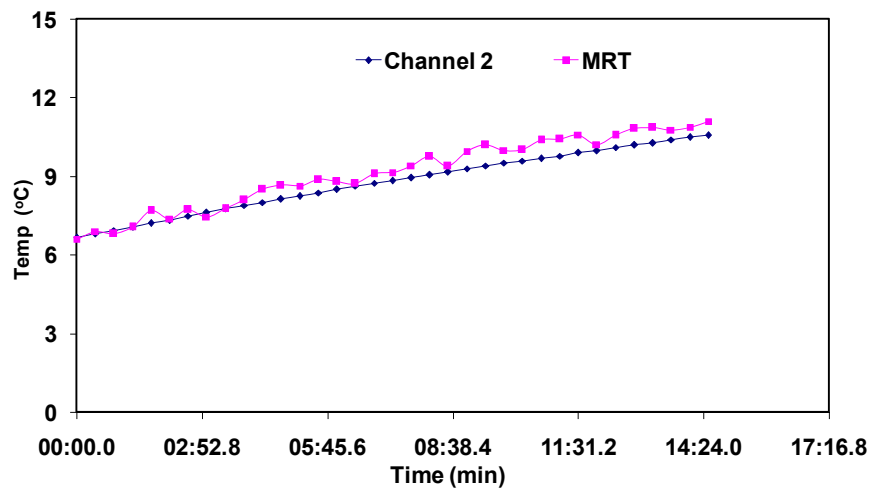


**Figure 4.13.** Temperature calibration of MRI using optical sensor for 1 average with TE = 4.296 ms, TR = 200 ms, 25.6 s/cycle, and IT = 3.56 °C.

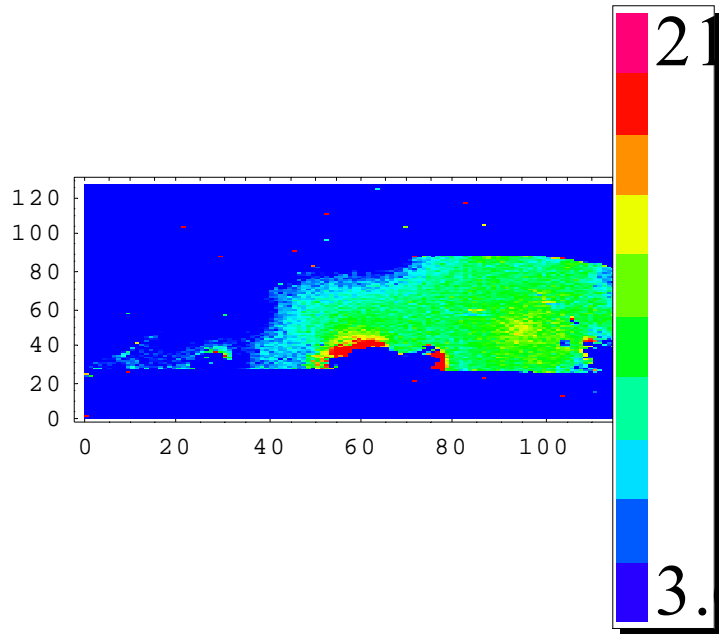


**Figure 4.14.** Temperature calibration profile mapping for chicken breast tissue with longer TE.

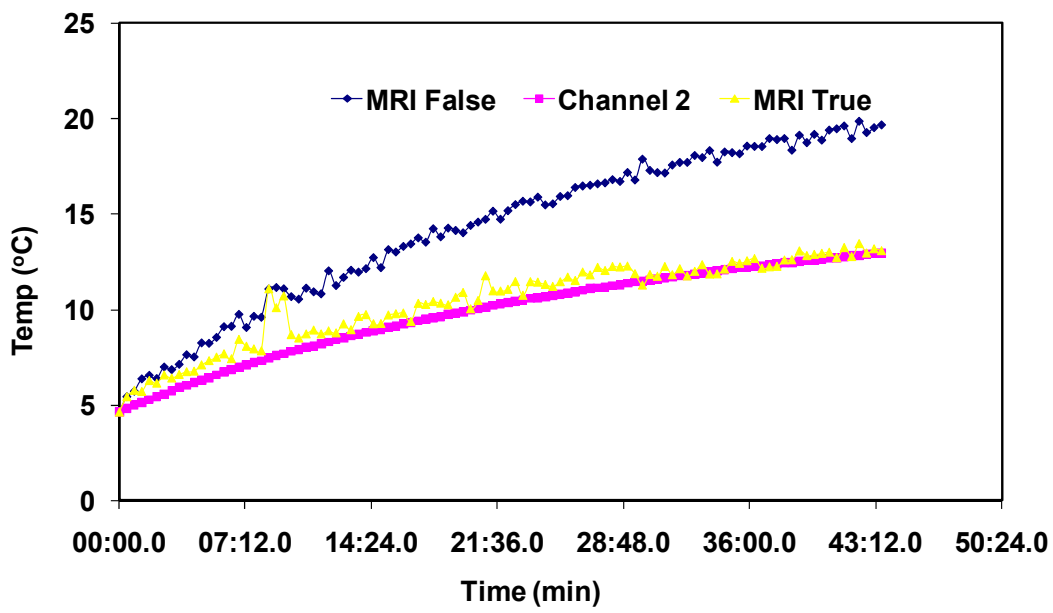


**Figure 4.15.** Graphical representation of susceptibility artifact effect.

Figure 4.15 compares the calibration results from two locations of the central slice (3/5). The parameters are for 1 average with TE = 3.935 ms, TR = 200 ms, 25.6 s/cycle, and IT = 5.8 °C. The artifact from Figure 4.16 is verified here as one can see the huge difference in temperature profile. It is worth noting that at approximately 8 minutes, the MRI 2 profile was exposed to the same systemic error that the MR profile was experiencing during the entire reading. Ultimately, the problem was solved by increasing Crushing Gradient/Spoiler power to eliminate accumulation residual transverse magnetization before the next excitation.

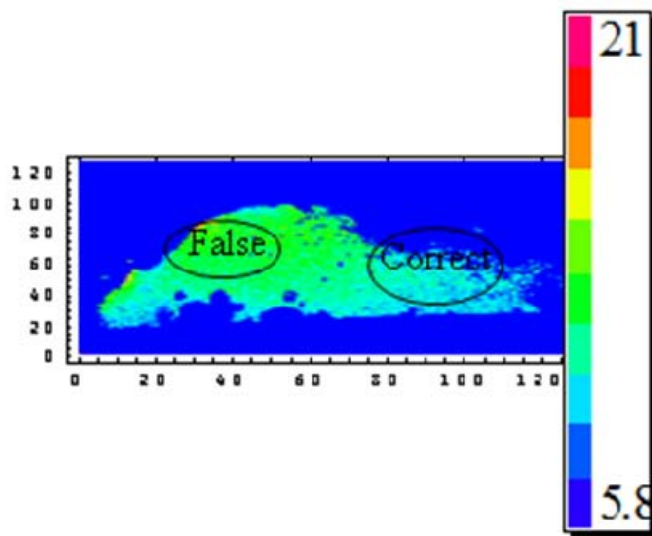


**Figure 4.16.** Temperature profiles in two different points in a chicken breast sample.

Figure 4.17 compares the calibration results from two locations of the central slice (3/5). The artifact from Figure 4.18 verified a huge difference in the temperature profile. At approximately 8 minutes, the mr2 profile was exposed to the same systemic error that the MR profile was experiencing during the entire reading (noted by the arrow). Slice

thickness was chosen to be 2 mm for the experiment. One can see a large saturation of artifact on the right portion of the chicken tissue. However, the data were not totally spoiled from the central to the outer left region.

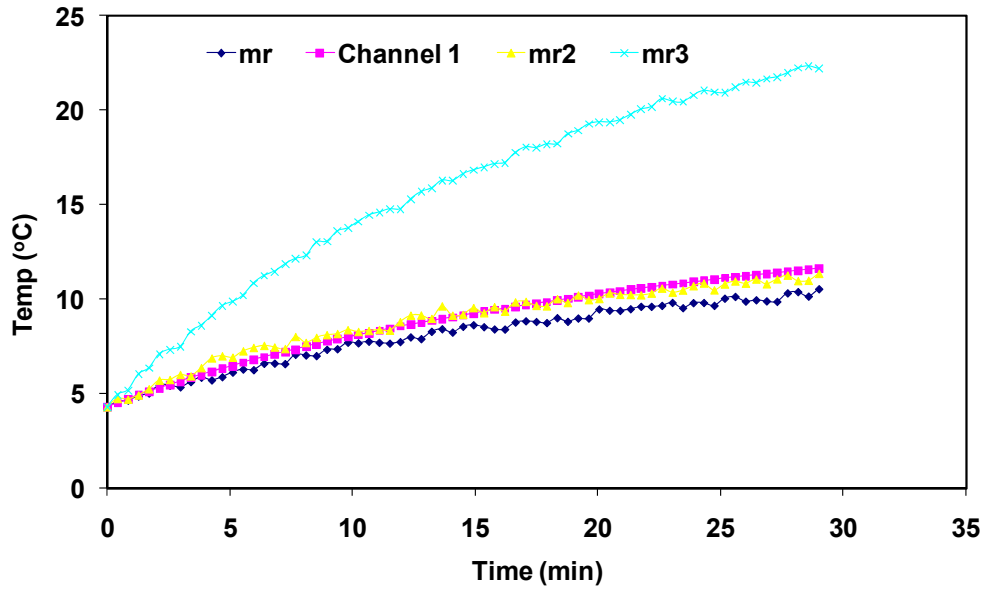


Figure 4.17. Susceptibility artifact and geometry selection.

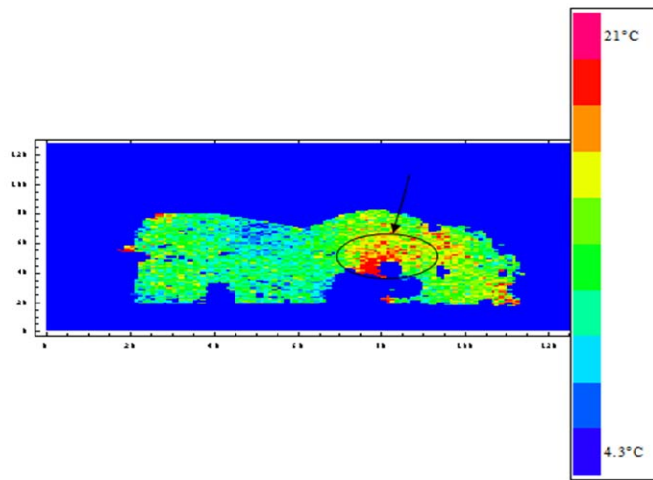
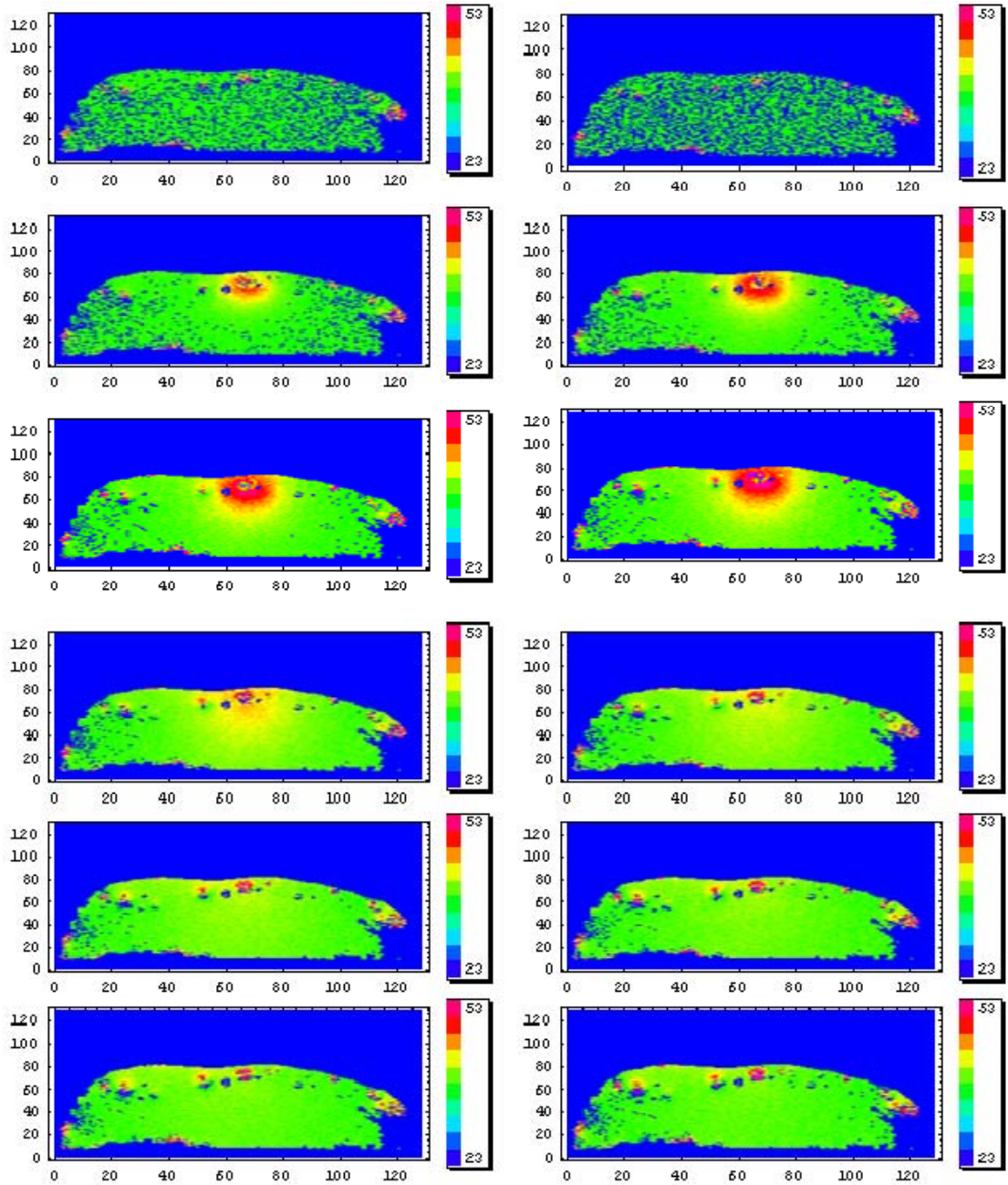
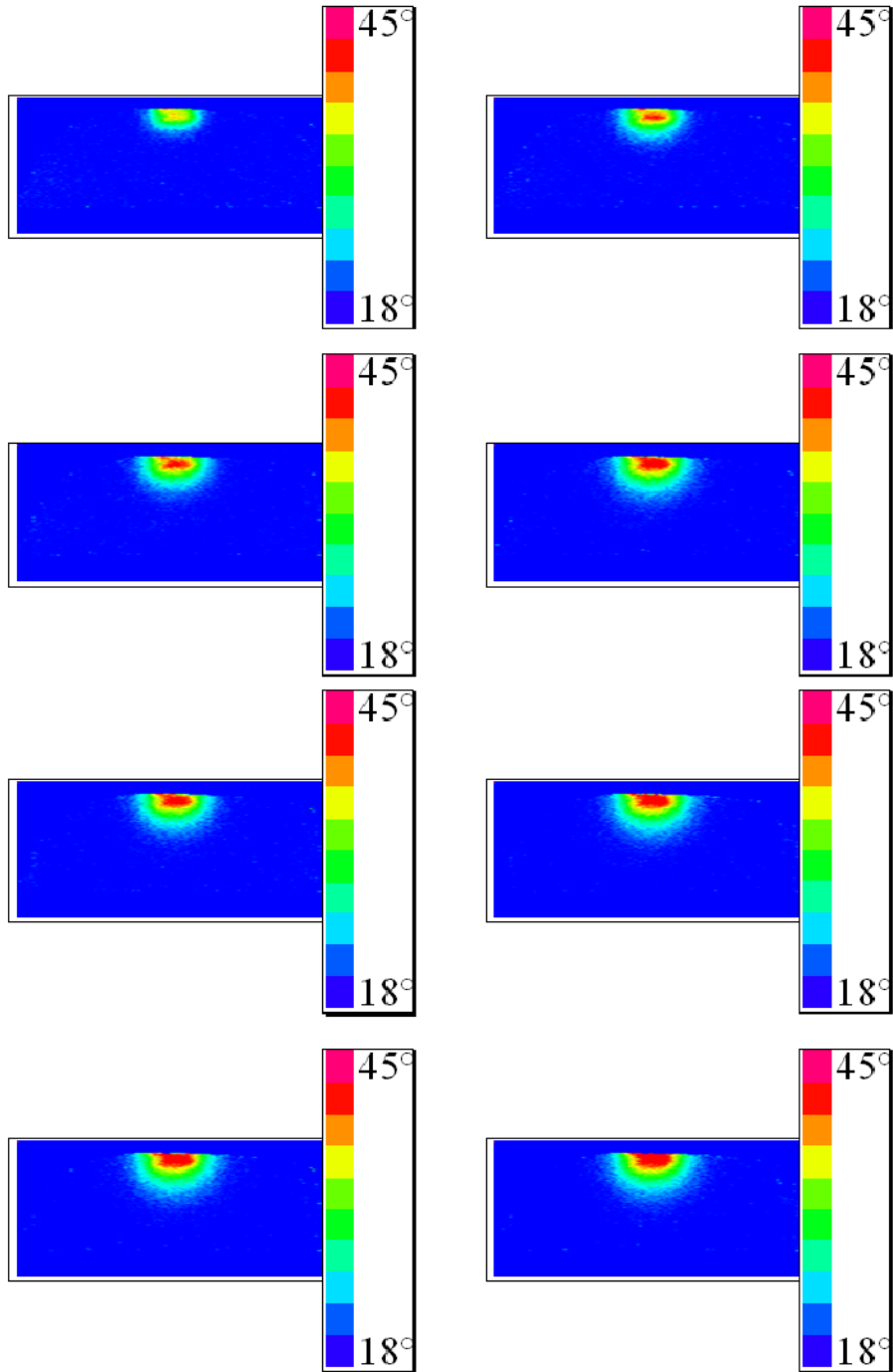


Figure 4.18. A temperature map profile in the latter stages of calibration.



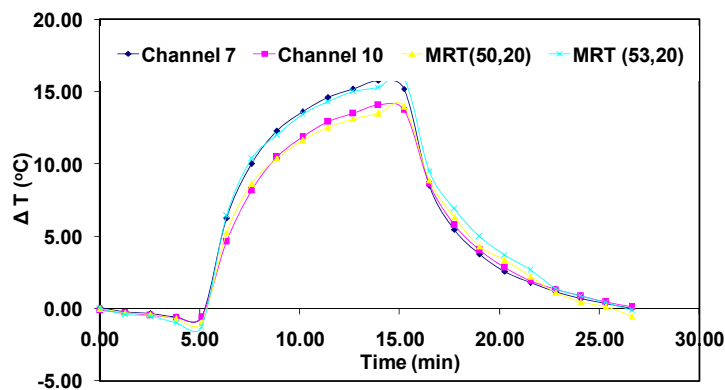
**Figure 4.19.** Temperature mapping of a 0.056% ICG concentrated dye ball embedded within the chicken breast tissue. The first plot is from an image after 304 sec and each successive image accounts for a 152 sec increment.



**Figure 4.20.** Temperature mapping of a 0.08% ICG concentrated chicken breast tissue. The first plot is from an image after 380 sec and each successive image accounts for a 76 sec increment.

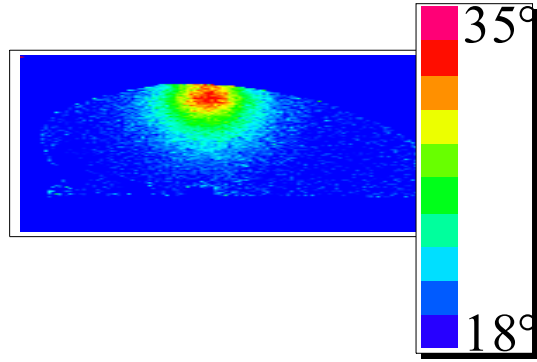
A gel containing a 0.056% ICG dye ball embedded within the chicken breast tissue temperature mapping versus time is shown in Figure 4.19. Temperature versus time of a chicken breast tissue injected with 0.2 mL 0.08 % ICG is shown in Figure 4.20. The sequence was plotted with a List Density Plot in Figure 4.19 and an Array Plot was used for Figure 4.20. Laser irradiation started on the center of the top surface of the tissue at 5 min after data initiation. The laser irradiation ended after a ten-minute period. The power density was  $1.0 \text{ W/cm}^2$ . The first image shown is 380 sec after data initiation with imaging dimensions of  $128 \times 128$  pixels. Each successive image is a 76 sec increment.

Figure 4.21 shows the temperature elevation using 0.08% ICG concentration with 3 averages. The echo time, TE, for this experiment was 3.935 ms and the scan time, TR, was 200 ms. The experiment was conducted with a 76 sec/cycle. The initial temperature was  $18^\circ\text{C}$ . From the graphical representation in Figure 4.21, one can see that the MRI data and the thermocouple measurements are matching; therefore, it is clear that the MRI can be used for 3D temperature mapping in a very consistent manner.



**Figure 4.21.** Temperature profiles using MRT and thermocouple under the same parameters.





**Figure 4.22.** Chicken tissue temperature mapping versus time with 0.056% ICG concentration for 3 averages.

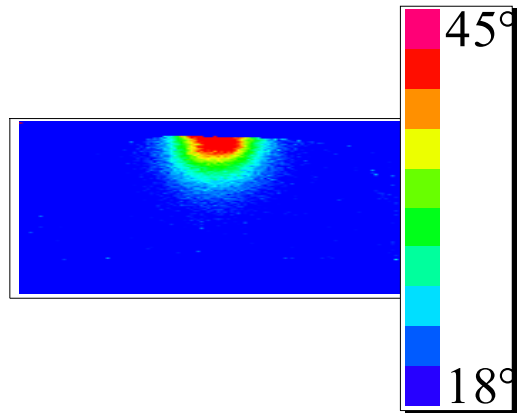


**Figure 4.23.** Chicken tissue temperature mapping versus time with 0.08 % ICG concentration for 3 averages.

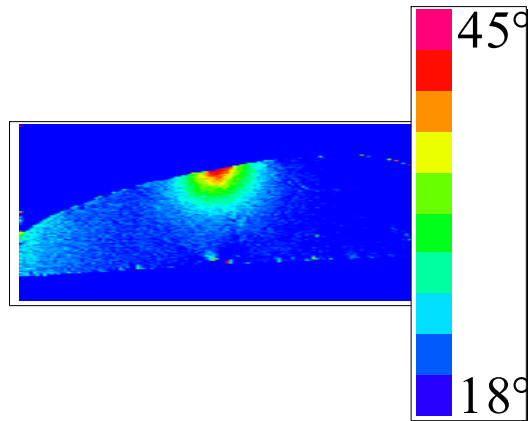


**Figure 4.24.** Chicken tissue temperature mapping versus time with 0.1 % ICG concentration for 3 averages.

Figures 4.22, 4.23, and 4.24 reflect the temperature distributions in chicken breast tissue with 0.056%, 0.08%, and 0.10% of ICG, respectively. All three experiments were performed with same parameters, except for the ICG concentrations. Figure 4.22 reflects that the temperature elevation ( $\Delta T$ ) is 15-17°C. From Figure 4.23, the raise in temperature ( $\Delta T$ ) is 25-30 °C and the temperature elevation is in the target region without harming the surrounding regions. In Figure 4.24, with a 0.10% of dye concentration, the figure depicts almost the same temperature elevation, but the temperature distribution is not only in the target region. For all three experiments, laser irradiation started on the center of the surfaces of the target tissue at 5 min after data initiation. The laser irradiation ended after a ten-minute period. The power density was 1.0 W/cm<sup>2</sup>. The image shown is the thirteenth cycle after data initiation with imaging dimensions of 128×128. The signal is clear due to the correct selection of number of excitations (NEX), which are three in this case. ICG with a 0.056% concentration showed more selectivity compared to that of an ICG with a 0.08% concentration. However, phantom gels with 0.08% of ICG showed a considerable temperature elevation of 10-35°C and temperature distribution.

## SECTION 5. DISCUSSIONS AND SUMMARY

Laser photothermal therapy is used for selective laser tissue interaction as its first line of assault on the tumor and then produces immunological stimulation for a long-term cure. A selective laser tissue interaction can be achieved using an 805 nm diode laser and intratumorally administered ICG. Laser energy can induce acute photothermal tissue damage and it can also serve as a precursor of immune responses. In addition, it can produce tumor-specific antigens and other immunological stimulation elements. Laser immunotherapy, using a combination of the laser thermal energy and immunological stimulation, has been successfully applied in the treatment of metastatic tumors. The dye-enhanced tumor-stimulating tissue below the surface can absorb more energy than the surface tissue. With appropriate laser power and beam size, the temperature in the dye-enhanced, deeper tissue can be increased more than normal, non-enhanced tissue.

This study focused on the precision of the MRT mapping with a better-known measuring reference thermocouple. The calibration samples were set at a constant temperature of 4°C, and then the temperature distributions of the samples were allowed to be measure simultaneously using the MRI system and the thermocouple. The two mappings can therefore be compared and calibrated accordingly.

Temperature mapping using MRT technique relies on the phase information and various parameters, from which the change in temperature can be deduced. MRT is a relatively new temperature mapping technique, and therefore, many unresolved issues can complicate the temperature measurement. However, some researchers have shown

that the precision of the temperature measurement is at the level of  $0.5^{\circ}\text{C}$  with a specialized technique using fat as reference [30-34, 42, 44, 82]. MR imaging has numerous advantages. It is a non-invasive, 3D mapping technique, and the effects of lasers on the tissue can be detected. In addition, optical fiber and light are not affected by the magnetic fields used for MR imaging, nor does optical fiber disturb the MR signal. At high temperatures, the 3D mapping can expect phase wrapping.

MRT is not always convenient due to the fact that it requires more time to set up all parameters; however, the result is well worth the wait. Amazingly, details of temperature distribution can be obtained, slice-by-slice, which is impossible using thermocouple only. Many effective algorithms have been developed, such as the L-norm method and the well-known Flynn's method, to solve the phase wraps dilemma [84-86]. Other details for conducting MRT include the subject is at constant temperature, high signal-to-noise ratio (SNR), and FLASH [87].

On the other hand, temperature mapping using thermocouple is highly sensitive and precise, up to  $0.01^{\circ}\text{C}$ . The thermocouples convert volts to temperature. This process is fairly simple and inexpensive to run. Beforehand, the probes need to be calibrated to ensure reliability. However, the mapping is not 3D and the accuracy of temperature reading on the surface is reduced due to the direct exposure of the thermocouples to the laser beam. On the contrary, MRT technique completely avoids the challenge of laser irradiation.

In this project, a new approach for the measurement of temperature distribution in target and non-target samples during irradiation with 805 nm Laser, was based on high sensitivity phase-difference MR thermometry, has been proposed and implemented. The

temperature distribution was determined using MRT (Figures 4.19, 4.20, and 4.21). One of the important experimental results was the confirmation of the chemical shift tissue near-independency of water proton, which was determined to be  $-0.01 \text{ ppm/}^\circ\text{C}$  with deviation of  $0.001 \text{ ppm/}^\circ\text{C}$  (Figure 4.9).

The goal of this study was to find out the optimal temperature distributions for thermal tissue interactions and to enhance immune responses in the target tissue. Temperature elevation with 0.056% of ICG and  $2.0 \text{ watt/cm}^2$  of laser power density showed better selectivity compared to that of 0.08% and 0.10% ICG (see Figure 4.19). However, phantom gels and chicken breast tissue with 0.08% of ICG and  $1.0 \text{ watt/cm}^2$  of laser power density showed a considerable temperature elevation of  $10\text{-}35^\circ\text{C}$  (Figure 4.22). The experimental results indicated the feasibility of an accurate, real-time 3D temperature mapping inside the tissue during laser treatment. When working with a high temperature elevation during laser irradiation, a lowest TE with the three NEX is optimal (as shown in Figures 4.22, 4.23 and 4.24). Further studies are needed to understand the precise thermal coefficient contributed by the susceptibility artifact. This study can lead to a method to monitor and guide laser cancer treatment.

It is a challenge to get even distribution of heat throughout the target region. Additional research is needed to learn more about the properties of the absorbent dye (ICG) and how it interacts with the targeted tissue and incident laser beam. Monitoring laser-tissue interaction using MRT is ideal for the measurement of adipose tissues, such as breast tissue, which can be used to investigate the temperature dependence of Photo-thermal interaction with tissue. One approach is to raise the temperature with laser and perform the imaging using MRT and optical sensor as well. By measuring the entire

thermal history throughout the experiment, one can give a measurement of tissue temperature distribution as a function of phase difference.

In conclusion, the accurate temperature distribution is a prerequisite for successful applications of the laser immunotherapy in the treatment of metastatic cancer. The MRT has been proven to be a feasible tool for the determination of temperature distribution. Our work sets up a stage for future studies using animals and could eventually lead to the effective use of laser immunotherapy in clinical settings.

## REFERENCES

1. Carlomagno C., Farella A., Buccci L., et al. Neo-adjuvant treatment of rectal cancer with capecitabine and oxaliplatin in combination with radiotherapy: a phase II study. *Ann Oncol*, 719, **2009**.
2. Rosenthal D. I., Catalano D.J., Haller D., et al. Phase I study of preoperative radiation therapy with concurrent infusional 5-fluorouracil and oxaliplatin followed by surgery and postoperative 5-fluorouracil plus leucovorin for T3/T4 rectal adenocarcinoma: ECOG E1297. *Int J Radiat Oncol Biol Phys*, 72, 108–13, **2008**.
3. Shivnani A.T., Small Jr. W., Stryker S.J., et al. Preoperative chemoradiation for rectal cancer: results of multimodality management and analysis of prognostic factors. *Am J Surg*, 193,389–93, **2007**.
4. Lefebvre JL, Rolland F, Tesselaar E, et al. Phase 3 randomized trial on larynx preservation comparing sequential vs. alternating chemotherapy and radiotherapy. *J Natl Cancer Inst*, 460, **2009**.
5. Posner M, Vermorken JB. Induction therapy in the modern era of combinedmodality therapy for locally advanced head and neck cancer. *Semin Oncol*, 35,221–8, **2008**.
6. Nagai K, Tsuchiya R, Mori T, et al. Lung cancer surgical study group of the Japan clinical oncology group. A randomized trial comparing induction chemotherapy followed by surgery with surgery alone for patients with stage IIIA N2 non-small cell lung cancer. *J Thorac Cardiovasc Surg*, 125, 254–60, **2003**.

7. Chau I, Brown G, Cunningham D, et al. Neoadjuvant capecitabine and oxaliplatin followed by synchronous chemoradiation and total mesorectal excision in magnetic resonance imaging-defined poor-risk rectal cancer. *J Clin Oncol*, 24, 668–74, **2006**.
8. K. Camphausen, M.A. Moses, W.D. Beecken, M.K. Khan, J. Folkman, and M.S. O'Reilly, Radiation therapy to a primary tumor accelerates metastatic growth in mice, *Cancer Res.* 61, 2207-11, **2001**.
9. W.H. Clark Jr., D.E. Elder, D.I.V. Guerry, L.E. Braitman, B.J. Trock, D. Schultz, M. Synnestevdt, and A.C. Halpern, Model predicting survival in stage I melanoma based on tumor progression, *J. Natl. Cancer Inst.* 81, 1893-1904, **1989**.
10. M.S. O'Reilly, R. Rosenthal, E. Sage, S. Smith, L. Holmgren, M.A. Moses, Y. Shing, and J. Folkman, The suppression of tumor metastases by a primary tumor, *Surg. Forum.* 44, 474-476, **1993**.
11. Sean O. Ryan Kira R. Gantt Olivera J. Finn, Tumor Antigen-Based Immunotherapy and Immunoprevention of Cancer, *Int Arch Allergy Immunology*, 142, 179–189, **2007**.
12. Wei R. Chen, Hong Liu, Jerry W. Ritchey, Kenneth E. Bartels, Michael D. Lucroy, and Robert E. Nordquist, Effect of Different Components of Laser Immunotherapy in Treatment of Metastatic Tumors in Rats<sup>1</sup>, *Cancer Research*, 62, 4295-4299, **2002**.
13. W.R. Chen, R.L. Adams, R. Carubelli, and R.E. Nordquist, Laser-photosensitizer assisted immunotherapy: A novel modality in cancer treatment, *Cancer Lett.* 115, 25-30, **1997**.
14. W.R. Chen, R. Carubelli, H. Liu, and R.E. Nordquist, Laser Immunotherapy: A Novel Treatment Modality for Metastatic Tumors, *Mol. Biotechnol.* 25, 37-43, **2003**.



15. W.R. Chen, W.G. Zhu, J.R. Dynlacht, H. Liu, and R.E. Nordquist, Long-term tumor resistance induced by laser photo-immunotherapy, *Int. J. Cancer* 81, 808-812, **1999**.
16. W.R. Chen, A.K. Singhal, H. Liu, and R.E. Nordquist, Laser immunotherapy induced antitumor immunity and its adoptive transfer, (Advances in Brief) *Cancer Research*. 61, 459-461, **2001**.
17. W.R. Chen, J.W. Ritchey, K.E. Bartels, H. Liu, and R.E. Nordquist, Effect of different components of laser immunotherapy in treatment of metastatic tumors in rats, *Cancer Research*. 62, 4295-4299, **2002**.
18. W.R. Chen, S.W. Jeong, M.D. Lucroy, R.F. Wolf, E.W. Howard, H. Liu, and R.E. Nordquist, Induced anti-tumor immunity against DMBA-4 metastatic mammary tumors in rats using a novel approach, *Int. J. Cancer*, 107, 1053-1057, **2003**.
19. Chen, Yichao, Gyanwalib, Surya, Bjorlie, Jeremy, Andrienko, Kirill, Liu, Hong, Tesiram, Yasvir A., Abbott, Andrew, Towner, Rheal A., Tissue temperature distribution measurement and laser immunotherapy for cancer treatment, *Proceedings of SPIE - The International Society for Optical Engineering*, 6087, **2006**.
20. J.L. Boulnois, Photophysical processes in recent medical laser developments: a review, *Lasers Med. Sci.* 1, 47-66, **1986**.
21. S.L. Jacques, Laser-tissue interactions, *The Cancer Bulletin*. 41, 211-218, **1989**.
22. S. Thomsen, Pathologic analysis of photothermal and photomechanical effects of laser-tissue interactions, *Photochem Photobiol*, 53, 825-835, **1991**.
23. S.L. Jacques, Laser-tissue interactions. Photochemical, photothermal, and photomechanical, *Surg. Clin. North Am.* 72, 531-558, **1992**.

24. Wei R. Chen et al, Optimization of Selective Hyperthermia, *Journal of Biomedical Optics* 9(3), 648-654, **2004**.
25. L.J. Anghileri and J. Robert, Hyperthermia in Cancer Treatment, *CRC Press, Boca Raton, FL*, **1986**.
26. M.H. den Brok, R.P. Sutmuller, R. van der Voort, E.J. Bennink, C.G. Figdor, T.J. Ruers, and G.J. Adema, *In situ* tumor ablation creates an antigen source for the generation of antitumor immunity, *Cancer Res.* 64, 4024-4029, **2004**.
27. P.K. Chakravarty, A. Alfieri, E.K. Thomas, V. Beri, K.E. Tanaka, B. Vikram, and C. Guha, Flt3-ligand administration after radiation therapy prolongs survival in a murine model of metastatic lung cancer, *Cancer Res.* 59, 6028-6032, **1999**.
28. P.K. Chakravarty, C. Guha, A. Alfieri, V. Beri, Z. Niazova, N.J. Deb, Z. Fan, E.K. Thomas, and B. Vikram, Flt3L therapy following localized tumor irradiation generates long-term protective immune response in metastatic lung cancer: its implication in designing a vaccination strategy, *Oncology.* 70, 245-254, **2006**.
29. Viola et al, Referenceless PRF shift thermometry, *Magnetic Resonance in Medicine* 51(6), 1223-1231, **2004**.
30. Yichao Chen et al, Magnetic Resonance Imaging Guidance for Laser Photothermal Therapy, *Journal of Biomedical Optics* 13(4), 1-8, **2008**.
31. Kagayaki Kuroda, Non-invasive MR thermography using the water proton chemical shift, *Int. J. Hyperthermia* 21(6), 547-560, **2005**.
32. Chen Y, Gnyawali SC, Wu F, Liu H, Tesiram YA, Abbott A, Towner RA, Chen WR, Magnetic resonance imaging guidance for laser photothermal therapy, *Journal of biomedical optics*, 13(4), 044033, **2008**.

33. Chen, Yichao, Gnyawali, Surya C., Liu, Hong, Tesiram, Yasvir A., Abbott, Andrew, Towner, Rheal A., Chen, Wei R., Optics in Tissue Engineering and Regenerative Medicine MRI 3D tissue temperature distribution measurement, *Progress in Biomedical Optics and Imaging, Proceedings of SPIE*, 6439, **2007**.
34. Ishihara Y, Calderon A, Watanabe H, Mori K, Okamoto K, Suzuki Y, Sato K, Kuruda K, Nakagawa N, Tsutsumi S. A precise and fast temperature mapping method using the water proton chemical shift. *In: Proceedings of the Eleventh Annual Meeting of SMRM, Berlin*, p 4803, **1992**.
35. S.J. Graham, G.J. Stanisz, A. Kecojevic, M.J. Bronskill, R.M. Henkelman, Analysis of Changes in MR Properties of Tissues After Heat Treatment, *Magnetic Resonance in Medicine* 42:1061–1071, **1999**.
36. Robert D. Peters, R. Scott Hinks, and R. Mark Henkelman, Heat-Source Orientation and Geometry Dependence in Proton-Resonance Frequency Shift Magnetic Resonance Thermometry, *Magnetic Resonance in Medicine*, 41, 909–918, **1999**.
37. Handbook of MRI Pulse Sequences, Matt A. Bernstein, Kevin F. King, Xiaohong Joe Zhou. , *Elsevier Academic press*, **2004**.
38. Okuda S, Kuroda K, Oshio K, Mulkern RV, Colucci V, Morrison PR, Kainuma O, Jolesz FA. MR-based temperature monitoring for hot saline injection therapy, *J Magn Reson Imaging*. Aug;12(2):330-8, **2000**.
39. Kagayaki Kuroda, Yutaka Suzuki, Yasutoshi Ishihara, Kazuya Okamoto, Yoshinori Suzuki, Temperature Mapping Using Water Proton Chemical Shift Obtained with 3D-MRSI: Feasibility in Vivo, *Progress in Biomedical Optics and Imaging, Proceedings of SPIE*, 35, 20-29, **1996**.

40. J.C. Hindman, Proton Resonance shift of water in the gas and liquid states. *J Chem. Phys.*, 44(12), 4582-92, **1966**.
41. Magnetic Resonance Imaging Physical Principles and Applications, Vadim Kuperman, *Academic Press*, **2000**.
42. Kuroda K, Non-invasive MR thermography using the water proton chemical shift, *Int. J. Hyperthermia*, 21(6), 547-560, **2005**.
43. Tao Wu, Kurtis R. Kendell, Joel P. Felmlee, Bradley D. Lewis, and Richard L. Ehman, Reliability of water proton chemical shift temperature calibration for focused ultrasound ablation therapy, *Medical Physics*, 27, 221-24, **2000**.
44. Y. Ishihara and K. Kuroda, A precise and fast temperature mapping using water proton chemical shift, *Magnetic Resonance in Medicine* 34, 814-823, **1995**.
45. R.D.Peters, R.S.Hinks, and R-M-Henklemann, *Ex-vivo* Tissue-Type independence in Proton-Resonance Frequency Shift MR Thermometry, *Magnetic Resonance in Medicine*, **1998**.
46. T. Harth, T. Kahn, M. Rassek, B. Schwabe, H. Schwarzmaier, J. Lewin, and U. Kfodder, Determination of Laser-induced Temperature Distributions Using Echo-shifted Turbo-FLASH, *Magnetic Resonance in Medicine*, 38, 238-245, **1997**.
47. C.Hillenbrand, R-Loffler, and R-Deichmann, Temperature monitoring on a clinical scanner using a fast hybrid imaging technique, *Proceedings of ISMRM*, **1998**.
48. Bruno Quesson, Jacco A. de Zwart, and Chrit T.W. Moonen, Magnetic Resonance Temperature Imaging for Guidance of Thermotherapy, *Journal of Magnetic Resonance Imaging* 12, 525-533, **2000**.

49. Delannoy J, Chen CN, Turner R, Levin RL, Le Bihan D. Noninvasive temperature imaging using diffusion MRI. *Magn Reson Med*, 19, 333–339, **1991**.
50. Hall AS, Prior MV, Hand JW, Young IR, Dickinson RJ. Observation by MR imaging of in vivo temperature changes induced by radio frequency hyperthermia. *J Comput Assist Tomogr*, 14, 430–436, **1990**.
51. Moseley M, Cohen Y, Mintorovitch J, Kucharczyk J, Weinstein P. Early detection of cerebral ischemia in cats: comparison of diffusion and T2-weighted MRI and spectroscopy. *Magn Reson Med* 14, 330, **1990**.
52. Brown, Mark A. Semelka, Richard C. , MRI: Basic Principles and Applications, *New York John Wiley & Sons, Inc. (US)*, **1999**.
53. Govind B Chavhan, MRI made easy, *Jaypee Brothers Medical publishers (P) LTD*. **2007**.
54. Zang-hee Cho, Joie P. Jones, Manbir Singh, Foundation Of Medical Imaging, *John Wiley & Sons, Inc.* **1993**.
55. C.W. Song, A. Lokshina, J.G. Rhee, M. Patten, and S.H. Levitt, Implication of blood flow in hyperthermic treatment of tumors, *IEEE Trans Biomed Eng.* 31, 9-16, **1984**.
56. H.S. Reinhold and B. Endrich, Tumor microcirculation as a target for hyperthermia: A review, *Int. J. Hyperthermia* 2, 111-137 **1986**.
57. H.G. Zhang, K. Mehta, P. Cohen, and C. Guha, Hyperthermia on immune regulation: a temperature's story, *Cancer Lett.* 2, 191-204, **2008**.
58. W.C. Dewey, L.E. Hopwood, S.A. Sapareto, and L.E. Gerweck, Cellular responses to combinations of hyperthermia and radiation, *Radiology.* 123, 463-474, **1977**.

59. S.A. Sapareto and W.C. Dewey, Thermal dose determination in cancer therapy, *Int. J. Radiat. Oncol. Biol. Phys.* 10, 787-800, **1984**.
60. S.B. Field and C.C. Morris, The relationship between heating time and temperature: Its relevance to clinical hyperthermia, *Radiother. Oncol.* 1, 179-186, **1983**.
61. A.J. Thistlethwaite, D.B. Leeper, D.J. Moylan, and R.E. Nerlinger, pH distribution in human tumors, *Int. J. Radiat. Oncol. Biol. Phys.* 11, 1647-1652, **1986**.
62. M.W. Dewhurst, W.G. Conner, T.E. Moon, and H.B. Roth, Response of spontaneous animal tumors to heat and/or radiation: preliminary results of a phase III trial, *J. Natl. Cancer Inst.* 61, 395-397, **1982**.
63. M.W. Dewhurst, W.G. Conner, and D.A. Sim, Preliminary results of a phase III trial of spontaneous animal tumors to heat and/or radiation: early normal tissue response and tumor volume influence on initial response, *Int. J. Radiat. Oncol. Biol. Phys.* 8, 1951-1962, **1982**.
64. J.H. Kim, E.W. Hahn, and N. Tokita, Combination hyperthermia and radiation therapy for cutaneous malignant melanoma, *Cancer.* 41, 2143-2148, **1978**.
65. H.H. Leveen, S. Wapnick, V. Riccone, G. Falk, and N. Ahmed, Tumor eradication by radio-frequency therapy, *J. Am. Med. Assoc.* 235, 2198-2200, **1976**.
66. M.R. Manning, T.C. Cetas, R.C. Miller, J.R. Oleson, W.G. Conner, and E.W. Gerner, Results of a phase I trial employing hyperthermia alone or in combination with external beam or interstitial radiotherapy, *Cancer.* 49, 205-216, **1982**.
67. J.B. Marmor, D. Pounds, N. Hahn, and G.M. Hahn, Treating spontaneous tumors in dogs and cats by ultrasound induced hyperthermia, *Int. J. Radiat. Oncol. Biol. Phys.* 4, 967-973, **1978**.

68. J.B. Marmor, D. Pounds, D.B. Postic, and G.M. Hahn, Treatment of superficial human neoplasms by local hyperthermia induced by ultrasound, *Cancer*. 43, 196-205, **1979**.
69. W.R. Chen, R.L. Adams, S. Heaton, D.T. Dickey, K.E. Bartels, and R.E. Nordquist, Chromophore-enhanced laser-tumor tissue photothermal interaction using 808 nm diode laser, *Cancer Lett.* 88, 15-19, **1995**.
70. W.R. Chen, R.L. Adams, K.E. Bartels, and R.E. Nordquist, Chromophore-enhanced *in vivo* tumor cell destruction using an 808-nm diode laser, *Cancer Lett.* 94, 125-131 **1995**.
71. W.R. Chen, R.L. Adams, C.L. Phillips, and R.E. Nordquist, Indocyanine green *in situ* administration and photothermal destruction of tumor tissue using an 808-nm diode laser, *Proc SPIE* 2681, 94-101, **1996**.
72. W.R. Chen, R.L. Adams, A.K. Higgins, K.E. Bartels, and R.E. Nordquist, Photothermal effects on murine mammary tumors using indocyanine green and an 808-nm diode laser: An *in vivo* efficacy study, *Cancer Lett.* 98, 169-173, **1996**.
73. H.G. Zhang, K. Mehta, P. Cohen, and C. Guha, Hyperthermia on immune regulation: a temperature's story, *Cancer Lett.* 2, 191-204, **2008**.
74. X. Li, B. Beauviot, R. White, S. Nioka, B. Chance, and A. Yodh, Tumor localization using fluorescence of indocyanine green (ICG) in rat models, *Proc SPIE* 2389, 789-797, **1995**.
75. S. Zhao, M.A. O'Leary, S. Nioka, and B. Chance, Breast tumor detection using continuous wave light source, *Proc SPIE* 2389, 809-817 **1995**.

76. R.R. Anderson, C.A. Puliafito, E.S. Gragoudas, and R.F. Steinert, Dye enhanced laser photocoagulation of choroidal vessels, *Invest. Ophthalmol. Vis. Sci.* 25, 89, **1984**.
77. B. Jean, J. Maier, M. Braun, C.S. Kischkel, M. Baumann, and H.-J. Thiel, Target dyes in ophthalmology, Part I--principles and indications, *Lasers Light Ophthalmol.* 3, 39-45, **1990**.
78. C.A. Puliafito, T.K. Destro, and E. Dobi, Dye enhanced photocoagulation of choroidal neovascularization, *Invest. Ophthalmol. Vis. Sci.* 29, 414, **1988**.
79. J.H. Suh, T. Miki, A. Obana, K. Shiraki, M. Matsumoto, and T. Sakamoto, Indocyanine green enhancement of diode laser photocoagulation, *J. Eye* 7, 1697-1699, **1990**.
80. J.H. Suh, T. Miki, A. Obana, K. Shiraki, and M. Matsumoto, Effects of indocyanine green dye enhanced diode laser photocoagulation in non-pigmented rabbit eyes, *Osaka City Med. J.* 37, 89-106 **1991**.
81. Viola et al, Referenceless PRF shift thermometry, *Magnetic Resonance in Medicine* 51(6), 1223-1231, **2004**.
82. Yichao Chen et al, Magnetic Resonance Imaging Guidance for Laser Photothermal Therapy, *Journal of Biomedical Optics* 13(4), 1-8, **2008**.
83. Kagayaki Kuroda, Non-invasive MR thermography using the water proton chemical shift, *Int. J. Hyperthermia* 21(6), 547-560, **2005**.
84. J. C. Hindman, Proton resonance shift of water in the gas and liquid states, *J. Chem Phys.* 44(12), 4582-92, **1966**.
85. Sherman Braganza, Analysis of Phase-Unwrap Quality of OQM Images, <http://www.coe.neu.edu/~sbraganz/images>, **2006**.



86. Thomas J. Flynn, Two-dimensional phase unwrapping with minimum weighted discontinuity, *Optical Society of America*, 14, 2692-2701, **1997**.
87. Peter M. Jakob, Christian Hendrich, Thomas Breitling, Achim Schafer, Astrid Berdon, Real Time Monitoring of Laser-Induced Thermal Changes in Cartilage *in Vitro* by Using Snapshot FLASH, *MRM* 37, 805-808, **1997**.

**APPENDIX: TEMPERATURE CALIBRATION ALGORITHM USING**  
***MATHEMATICA 5.2<sup>TM</sup>***

# Calibration

## Algorithm June 30

2009 

- 1<sup>st</sup> Attempt Chicken Breast Calibration
- Room Temperature 21°C
- File # 2
- 25.6 s/cycle
- 422 total cycles
- 1 average
- SNR 14.8
- 7.0307 Tesla Coil
- TR 209 ms
- TE 3.95 ms
- Flip  $\Delta 30^\circ$

```
In[116]:= (*Blue color marks are for the user*)  
          (*Red color marks are important to note*)  
          (*Green color marks are synthetic functions*)  
          (*Press Alt Enter to start new cell*)
```

```
In[117]:= Needs["Graphics`"] ;  
          $HistoryLength = 0;
```

In[119]:=

In[120]:= (**\*User: enter the file paths below\***)

In[121]:= **filereal** = "F:\7\pdata\3\2dseq";

In[122]:= **fileimage** = "F:\7\pdata\4\2dseq";

In[123]:= **filemagnititude** = "F:\7\pdata\1\2dseq";

In[124]:= (**\*p and q are the step size of cycles;ex. from p=0 to q=50 which are 50 cycles selected etc.\***)

In[125]:= **p** = 0 ;  
**q** = 24 ;

In[127]:= **rate** = 25.6 ;  
**totalcycle** = 25 ;

In[129]:= **RoomT** = 21 ;

In[130]:= **InitialT** = 18

Out[130]= 18

In[131]:= 5

Out[131]= 5

In[132]:= (**\*the nth slice to be analyzed is slice\***)

In[133]:= **slice** = 10 ;

In[134]:= **d1** = 128 ;  
**d2** = 128 ;  
**d3** = 20 ;

In[137]:= (**\*TE is the echo time; shorter TE means less  $\Delta\phi$  for greater temperature change: good for avoiding the  $-\pi$  to  $\pi$  cap limit\***)

**TE** =  $3.935 * 10^{-3}$  ;

```
In[138]:= (*Here you can manually pick the x=h and y=gcoordinate to be analyzed*)
h = 60;
g = 60;
```

```
Out[138]= Null2
```

```
In[139]:= (*boxsize is a; boxsize determines the number of pixels to average*)
(*xo=h-k;
xt=h+k;
yo=g-k;
yt=g+k;*)
boxsize = k = 5;
```

```
In[140]:= (*aspect is obtained from the field of view ratio*)
aspect = .41;
```

```
In[141]:= (*lemit sets the threshold for masking using the magnitude file*)
lemit = 4000;
```

```
In[142]:= (*climax:the nth cycle where the laser ends if applicable*)
climax = 34;
```

```
In[143]:= (*The TopΔHeat is the estimated max ΔT*)
TopΔHeat = RoomT - InitialT;
```

```
In[144]:= (*L1 and L2 contain the initial cylce pixels to be partitioned*)
L1 = 1;
L2 = d1 * d2 * d3 * 1;
```

```
Out[144]= Null2
```

```
In[145]:= (*pixels from a to b contain the nth cycles*)
```

```
In[146]:= unit = 1;
a = d1 * d2 * d3 * p + unit;
b = d1 * d2 * d3 * q;
```

```
In[149]:= (*cycle is the cycles will be analyzed*)
cycle =  $\frac{(b + unit - a)}{(d1 * d2 * d3)}$ 
```

```
Out[149]= 24
```

```
In[150]:= (*totaltime is the time of the entire scan in minutes*)
```

```
In[151]:= totaltime =  $\frac{rate * totalcycle}{60}$ 
```

```
Out[151]= 10.6667
```

```
In[152]:= (*relativetime time from p to q in minutes*)
```

```
In[153]:= relativetime1 =  $\frac{\text{rate} * p}{60}$ 
relativetime2 =  $\frac{\text{rate} * q}{60}$ 
```

```
Out[153]= 0
```

```
Out[154]= 10.24
```

```
In[155]:= (*λ is the hydrogen gyromagnetic ratio*)
(*B is the Magnetic Strenth*)
(*α is the chemical shift per degree C*)
(*the master formula*)
(*ΔT=  $\frac{\Delta\phi}{\lambda * B * TE * \alpha}$  *)
```

```
In[156]:= λ = 2 * π * 42.67 * 10^6;
B = 7.0307;
TE;
α = -.010 * 10^-6;
```

```
In[160]:= (*μ is a constant*)
μ = λ * B * TE * α
```

```
Out[160]= -0.074173
```

```
In[161]:= (*The max ΔT without phase wrap is π/μ*)
```

```
In[162]:= maxΔT =  $\frac{-\pi}{\mu}$ 
```

```
Out[162]= 42.3549
```

```
In[163]:= (*the following funcitons may be useful such as
for finding the location of the max temperature increase*)
```

```
In[164]:= PL[data_] :=
ListPlot[data, PlotStyle -> {PointSize[.02], Hue[.1]}, PlotJoined -> True,
Ticks -> {Range[34], Automatic}, AxesLabel -> {"Phases", "Temp"},
PlotLabel -> "TYPE HERE", TextStyle -> {FontSize -> 14}];
```

```
In[165]:= func[Mlist_, cycle_, x1_, x2_, y1_, y2_] :=
Table[Take[Mlist[[i]], {y1, y2}, {x1, x2}], {i, 1, cycle}]
```

```
In[166]:= Tracker[M_, y_, x_] :=
Table[Take[M[[i]], {y-1, y+1}, {x-1, x+1}], {i, 1, cycle}];
```

```
In[167]:= CO[phase_, a_, b_] := Count[ADF[phase], _?(a < # < b &), 2];
```

```

In[168]:= edger[data_?MatrixQ, bounds_?VectorQ] :=
Module[{matrix, dimI, diJJ, lobound, hibound,
  replaced, rriiplaced, clipped}, matrix = data;
dimI = Dimensions[matrix][[1]];
diJJ = Dimensions[matrix][[2]];
lobound = bounds[[1]];
hibound = bounds[[2]];
replaced = ReplacePart[matrix, lobound, {1, 1}];
rriiplaced = ReplacePart[replaced, hibound, {2, 1}];
clipped = Map[Which[# ≥ hibound, hibound, # ≤ lobound,
  lobound, lobound < # < hibound, #] &, rriiplaced, {2}]
];

In[169]:= AVERAGE[square_] := Table[Mean[Flatten[square[[i]]]], {i, 1, cycle}];

In[170]:= (*The following commands decompose large
file into manageable size in nth cycle step size*)

In[171]:= fre = Take[BinaryReadList[filereal, "Integer16"], {a, b}];

In[172]:= fim = Take[BinaryReadList[fileimage, "Integer16"], {a, b}];

In[173]:= (*the following partition the nth cycles *)
d2r = Partition[Partition[Partition[If[# == 0, 1, #] & /@ fre, d1], d2], d3];
d2i = Partition[Partition[Partition[If[# == 0, 1, #] & /@ fim, d1], d2], d3];

In[175]:= (*The following take and partition the pixels from the initial cycle*)
d2roψ = Partition[Partition[Partition[If[# == 0, 1, #] & /@
  Take[BinaryReadList[filereal, "Integer16"], {L1, L2}], d1], d2], d3];
d2ioϖ = Partition[Partition[Partition[If[# == 0, 1, #] & /@
  Take[BinaryReadList[fileimage, "Integer16"], {L1, L2}], d1], d2], d3];
d2mω = Partition[Partition[Partition[If[# == 0, 1, #] & /@
  Take[BinaryReadList[filemagnitude, "Integer16"], {a, b}], d1], d2], d3];

In[178]:= (*the followings extract the nth slice usually the middle but you decide*)
real1 = d2roψ[[1]][[slice]];
real2 = Table[d2r[[i]][[slice]], {i, 1, cycle, 1}];
image1 = d2ioϖ[[1]][[slice]];
image2 = Table[d2i[[i]][[slice]], {i, 1, cycle, 1}];
(*The following equation is from the handbook of mri pulse sequence*)

In[182]:= AD = Table[ArcTan[(real1 * real2[[u]] + image1 * image2[[u]]),
  (real2[[u]] * image1 - real1 * image2[[u]])], {u, 1, cycle, 1}];

In[183]:= Dimensions[AD]
Out[183]:= {24, 128, 128}

```

```

In[184]:= Dimensions[d2mow]
Out[184]= {24, 20, 128, 128}

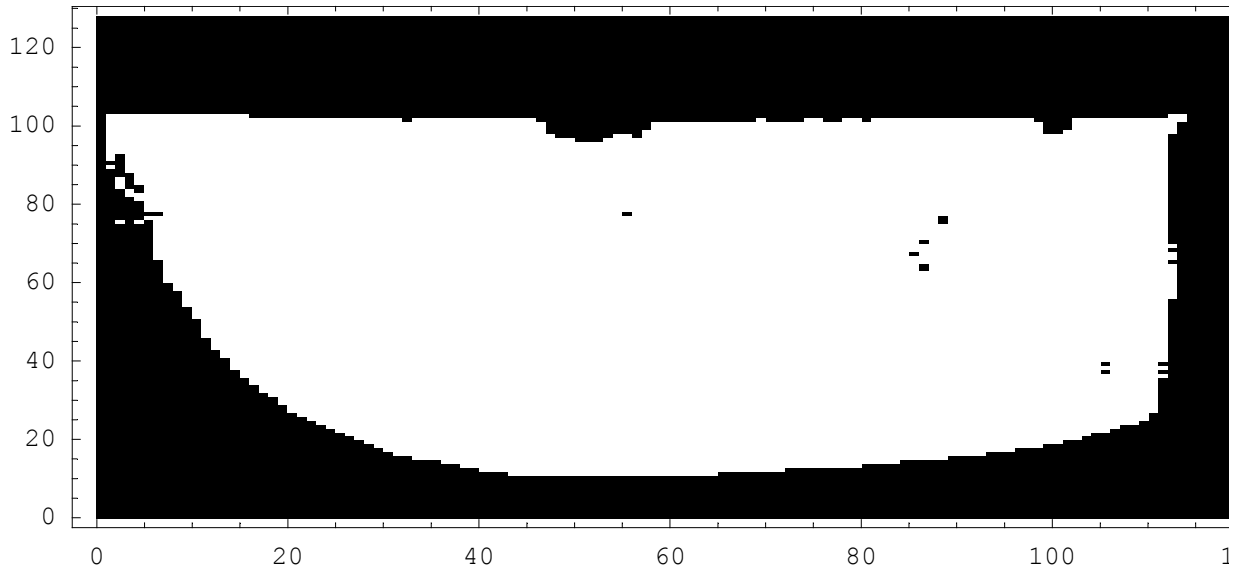
In[185]:= filter = d2mow[[1]][[slice]];
Dimensions[filter]
Out[186]= {128, 128}

In[187]:= thres = If[# > 5000, 1., 0] &;

In[188]:=

In[189]:= woolmesh = Map[thres, filter, {2}];
ListDensityPlot[woolmesh, PlotRange -> All, Mesh -> False, AspectRatio -> aspect];

```



```

In[191]:= Dimensions[woolmesh]
Out[191]= {128, 128}

In[192]:= Dimensions[AD]
Out[192]= {24, 128, 128}

In[193]:= (*Δφ is the masked product*)
Δφ = Table[AD[[p]] * woolmesh, {p, 1, cycle, 1}];

In[194]:= Dimensions[Δφ]
Out[194]= {24, 128, 128}

In[195]:= Min[Δφ];
Max[Δφ];

```



```

In[197]:= (*systemically pick x and y coordinate to be analyzed;
the default option is on hold*)

In[198]:= Hold[data1 = Table[
  Position[ $\Delta\phi$ [[p]], _? (-Pi .90 < # < -Pi * .30 &), 2], {p, climax - 6, climax + 2}];
num = Round[Map[Mean, data1, 1]];
Dimensions[num];
poose = Position[num, _? (0 < # < (d1 + 1) &)];
leng = Dimensions[poose][[1]];
width = Dimensions[poose][[2]];
posy = Table[poose[[i]][[1]], {i, 1, leng}];
y1 = Min[posy];
y2 = Max[posy];
data2 = Take[num, {y1, y2}];
num;
TM = totalmean = Round[Mean[data2]]
a = boxsize;
g = TM[[1]];
h = TM[[2]];];

In[199]:= xo = h - k;
xt = h + k;
yo = g - k;
yt = g + k;

In[203]:= (*box2 contains the phase change for selected pixels*)

In[204]:= box2 = func[ $\Delta\phi$ , cycle, xo, xt, yo, yt];
Dimensions[box2]

Out[205]= {24, 11, 11}

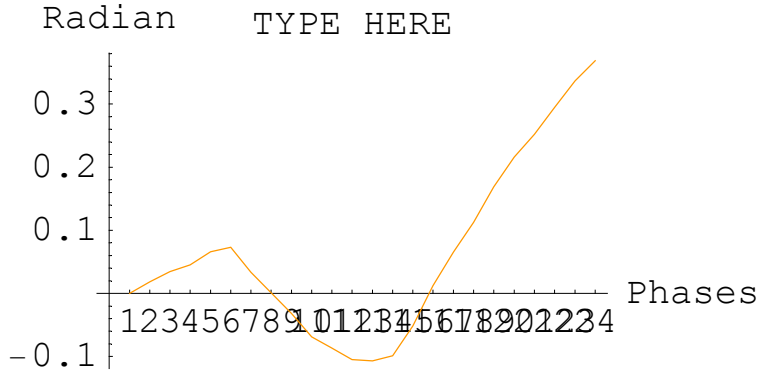
In[206]:= (*datanew is the set of averaged pixels*)

```

```

In[207]:= datanew = AVERAGE [box2] ;
          PL[data_] :=
            ListPlot[data, PlotStyle -> {PointSize[.02], Hue[.1]}, PlotJoined -> True,
              Ticks -> {Range[34], Automatic}, AxesLabel -> {"Phases", "Radian"},
              PlotLabel -> "TYPE HERE", TextStyle -> {FontSize -> 14}];
          PL[datanew];
          Null

```



```

In[211]:= (*the equation below converts phase change to temperature change*)

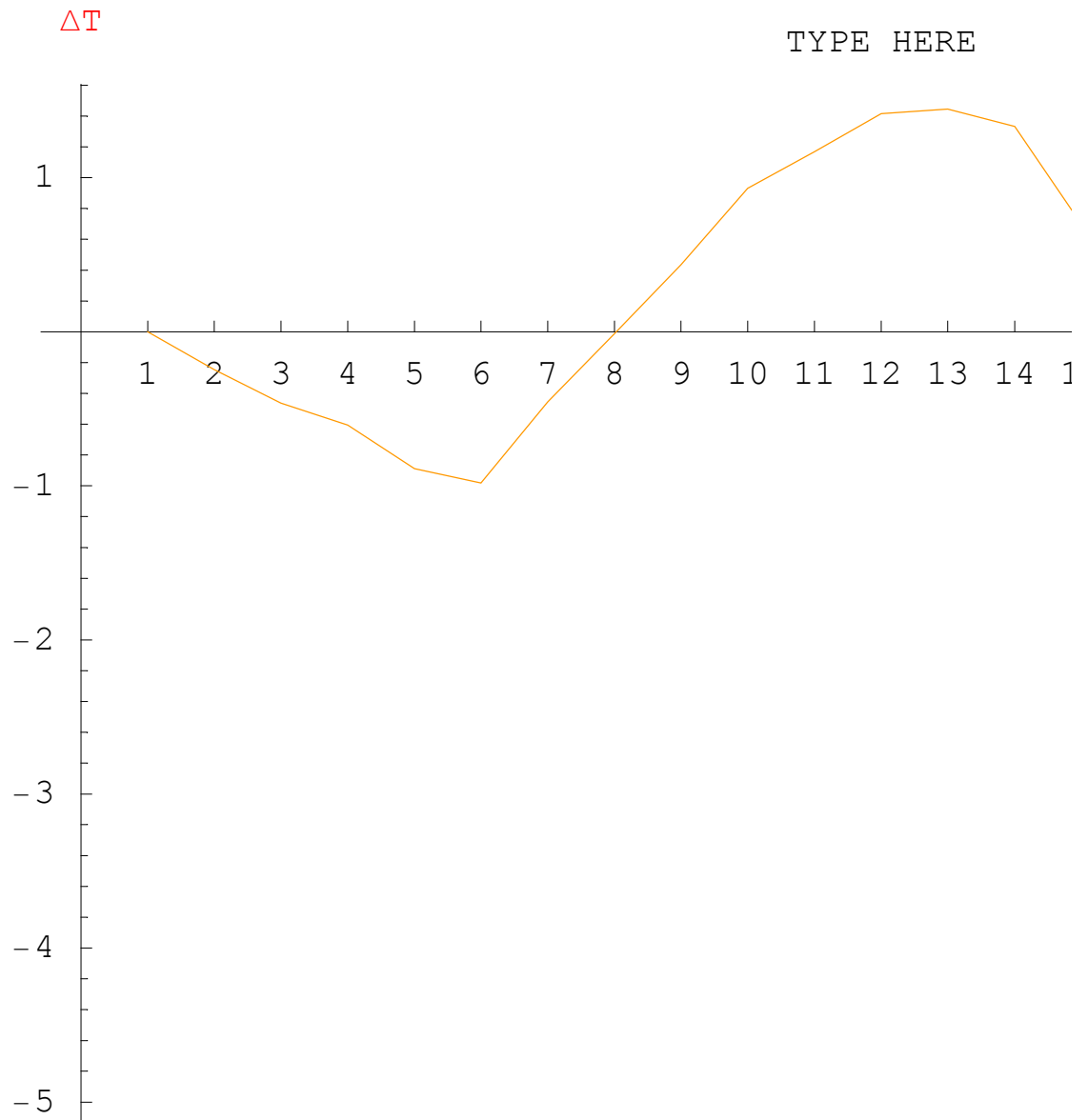
```

$$\text{In[212]:= } \Delta T = \frac{\Delta \phi}{\lambda * B * TE * \alpha} ;$$

```

In[213]:= box4 = func[ΔT, cycle, xo, xt, yo, yt];
          Dimensions[box4];
          (*datafinal is the final
            product: the ΔT as a single point through the cycles*)
          datafinal = AVERAGE [box4] ;
          PL[data_] :=
            ListPlot[data, PlotStyle -> {PointSize[.02], Hue[.1]}, PlotJoined -> True,
              Ticks -> {Range[34], Automatic}, AxesLabel -> {"Phases", "ΔT"},
              PlotLabel -> "TYPE HERE", TextStyle -> {FontSize -> 14}];
          PL[datafinal]
          Null

```



Out[217]= - Graphics -

```
In[219]:= (*TopHeat is only a approximate value;
the user can manually place the input value*)
TopHeat = RoomT - InitialT
```

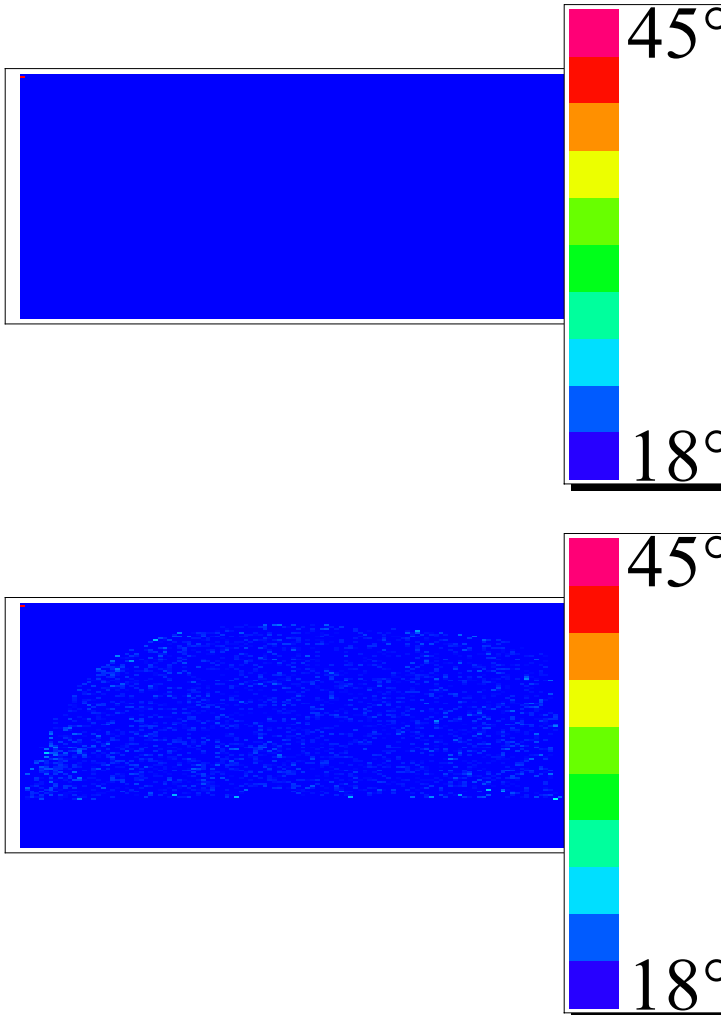
Out[219]= 3

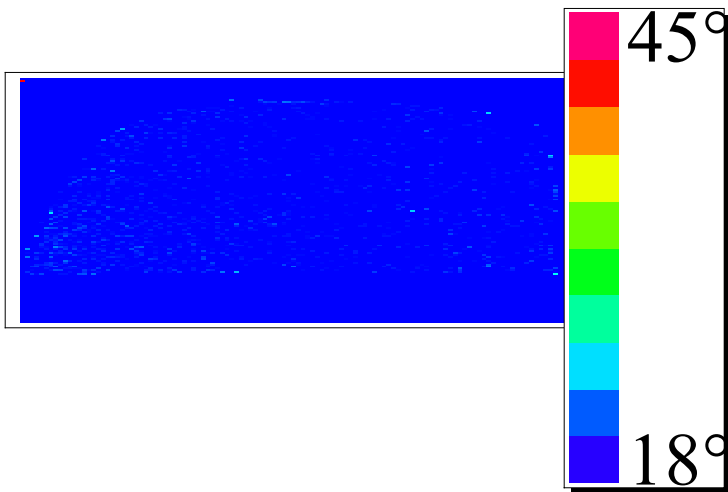
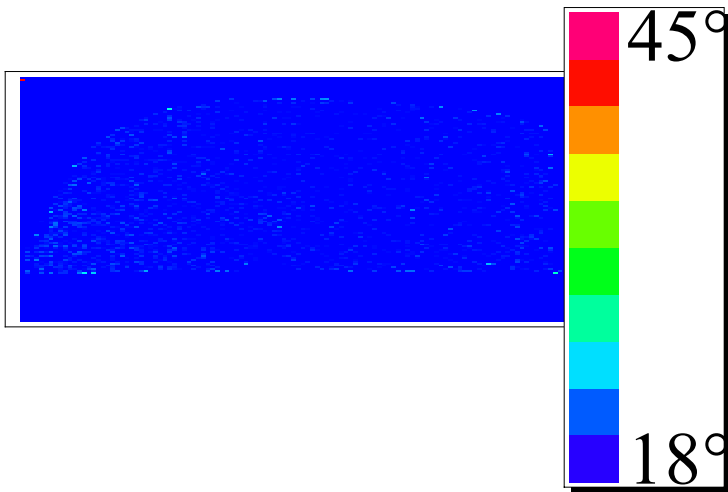
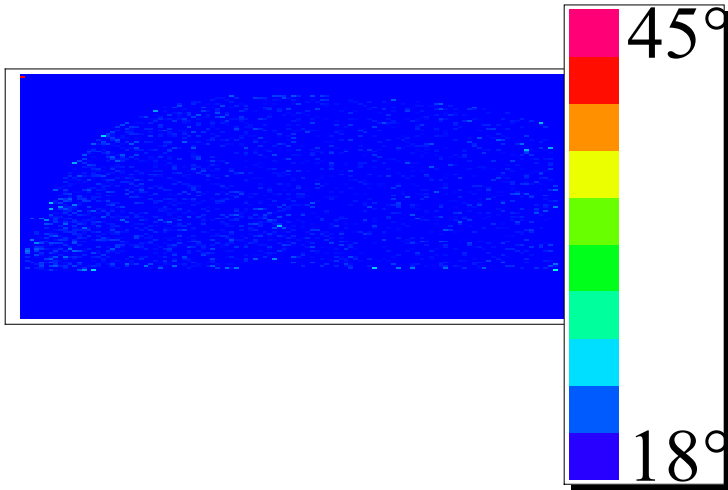
```
In[220]:= (*3 D mappings*)
```

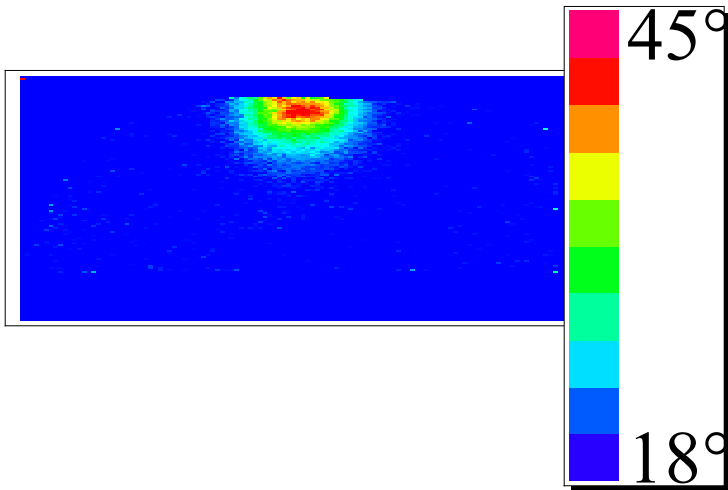
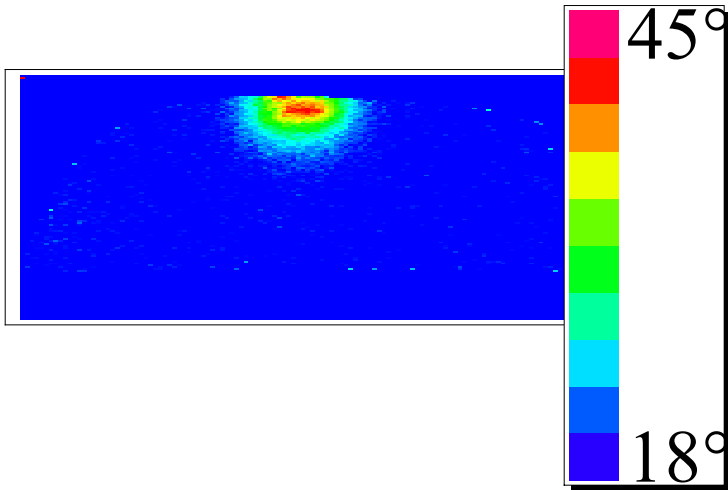
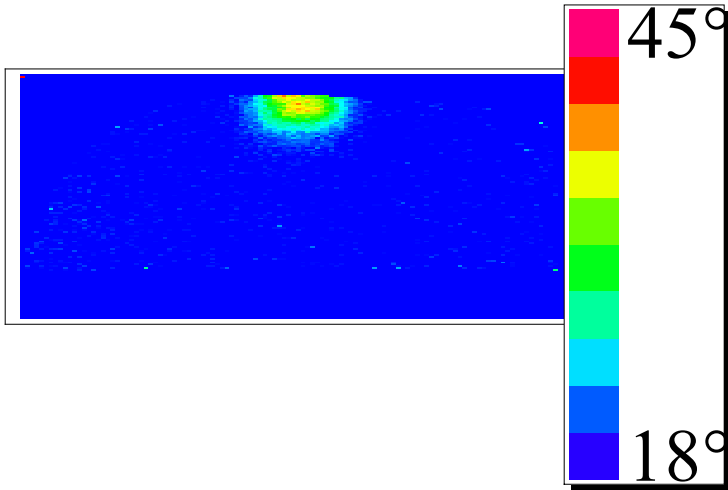
```

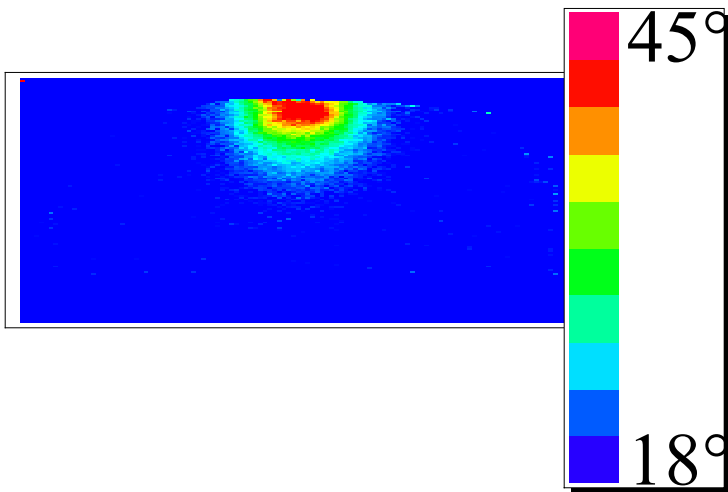
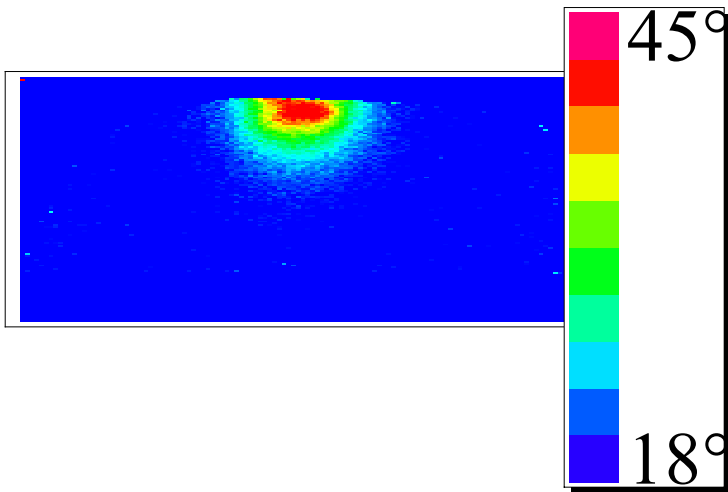
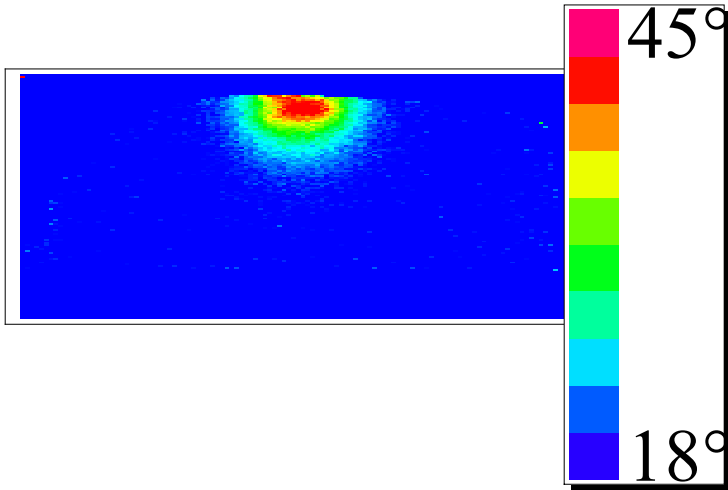
In[221]:= Table[ShowLegend[
  ArrayPlot[edger[ $\Delta T$ [[k]], {0, 25}], PlotRange  $\rightarrow$  All, AspectRatio  $\rightarrow$  .4,
  ColorFunction  $\rightarrow$  (Hue[(2.5 - #) / 1.5] &), ColorOutput  $\rightarrow$  Automatic,
  Mesh  $\rightarrow$  False, ColorFunctionScaling  $\rightarrow$  True, DisplayFunction  $\rightarrow$  Identity],
{Hue[(2.5 + #) / 1.3] &, 10, "45°C", "18°C", LegendPosition  $\rightarrow$  {.75, -.9},
  LegendSize  $\rightarrow$  {.5, 1.5}, LegendShadow  $\rightarrow$  {0.02, -0.02}},
  TextStyle  $\rightarrow$  {FontFamily  $\rightarrow$  "Times", FontSize  $\rightarrow$  28}], {k, 1, cycle, 1}];

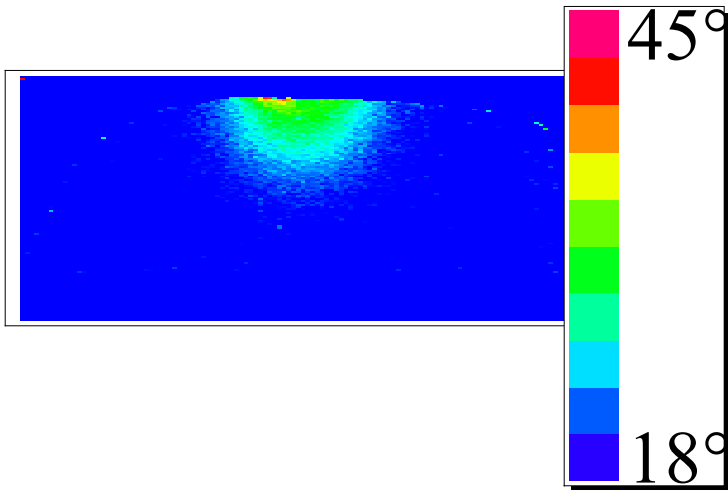
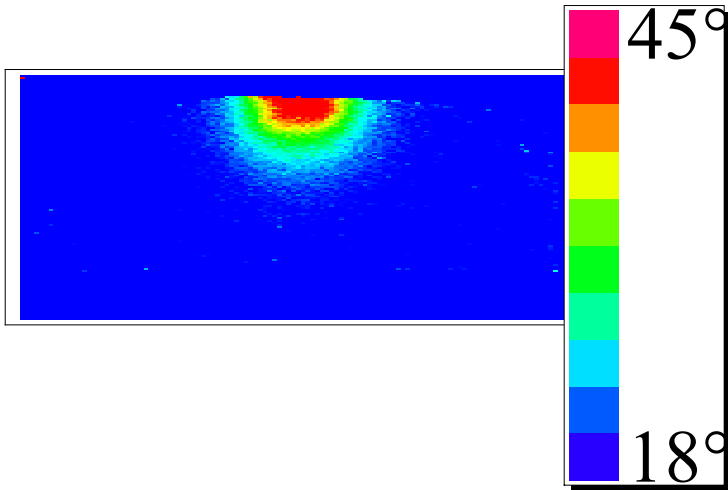
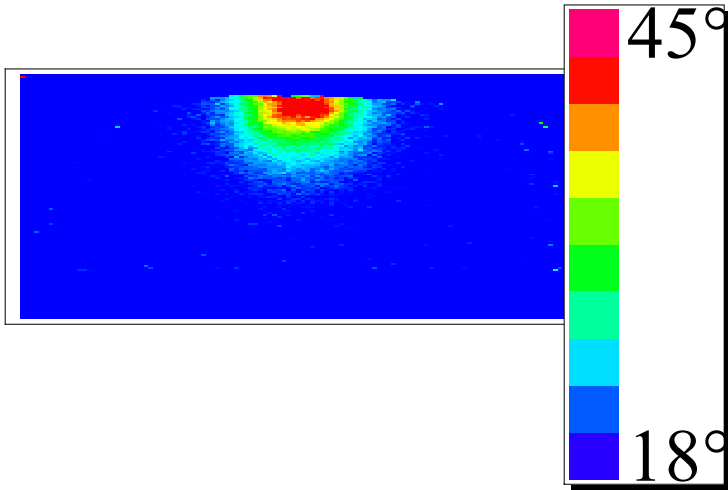
```



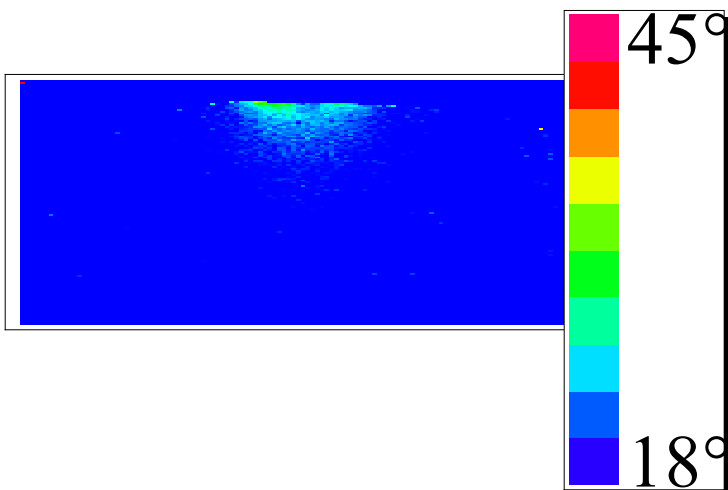
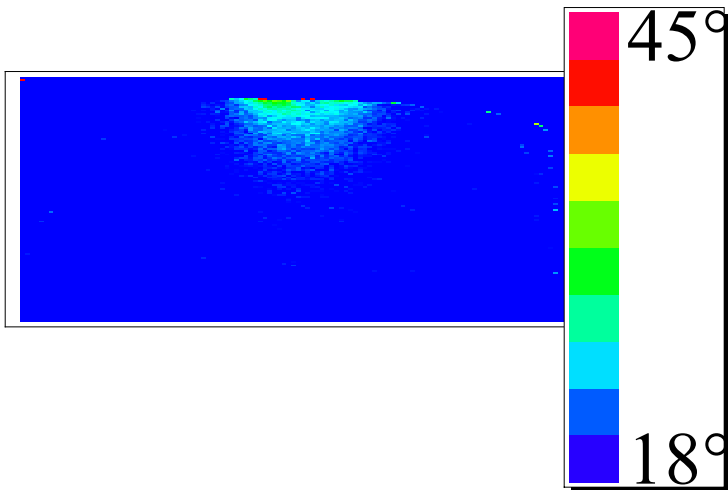
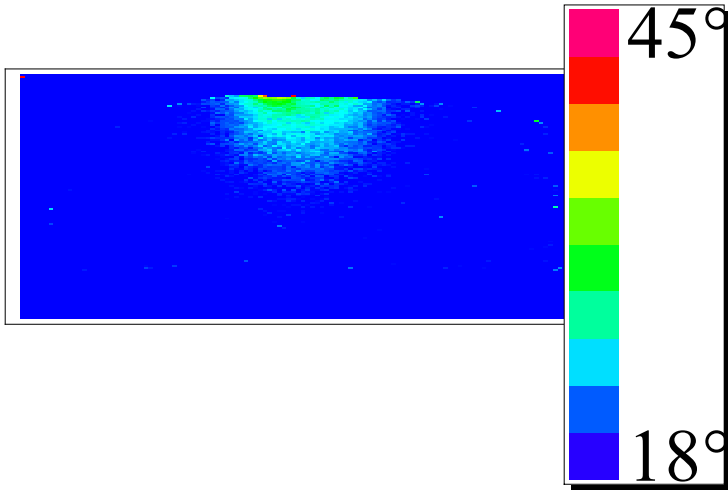


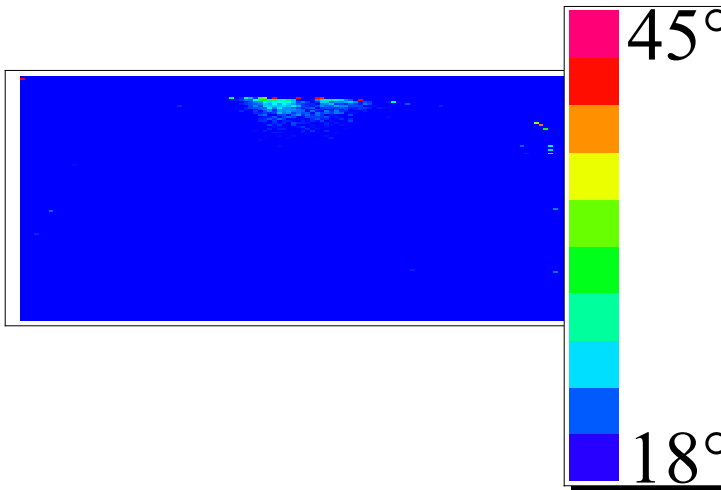
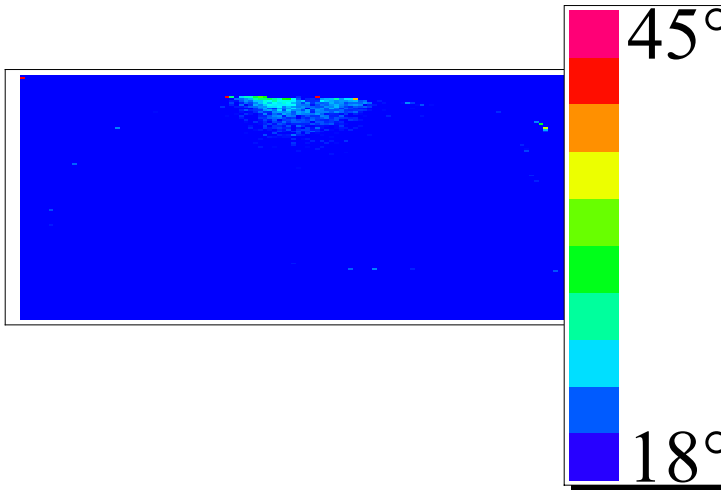
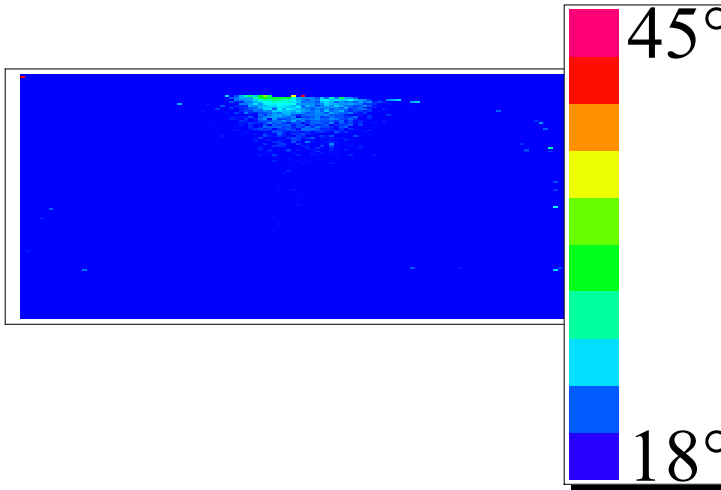


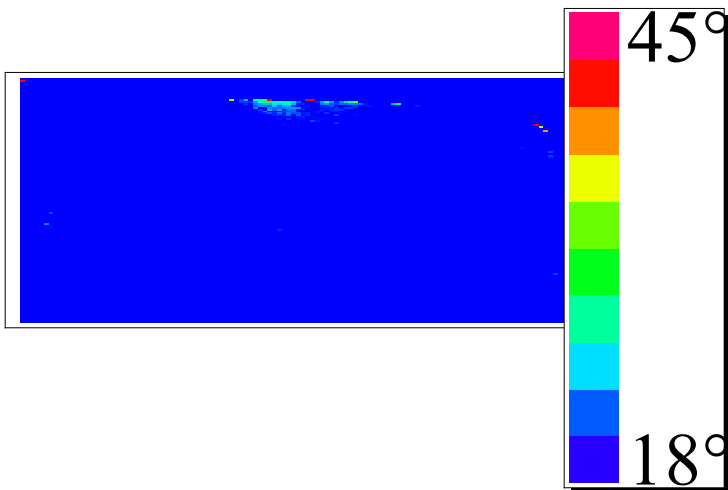
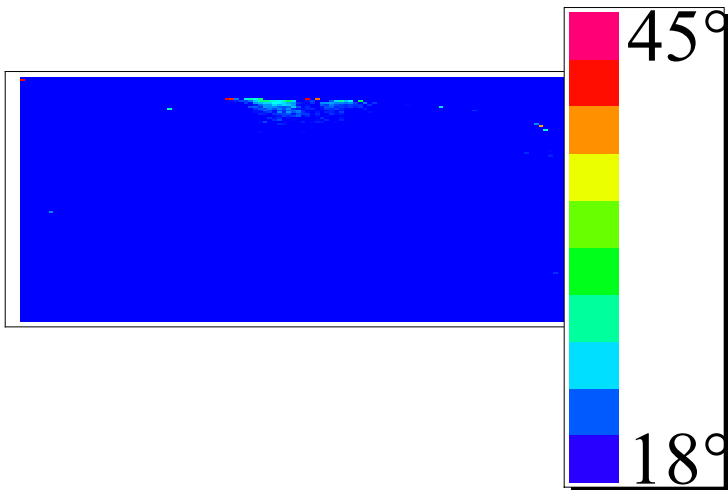
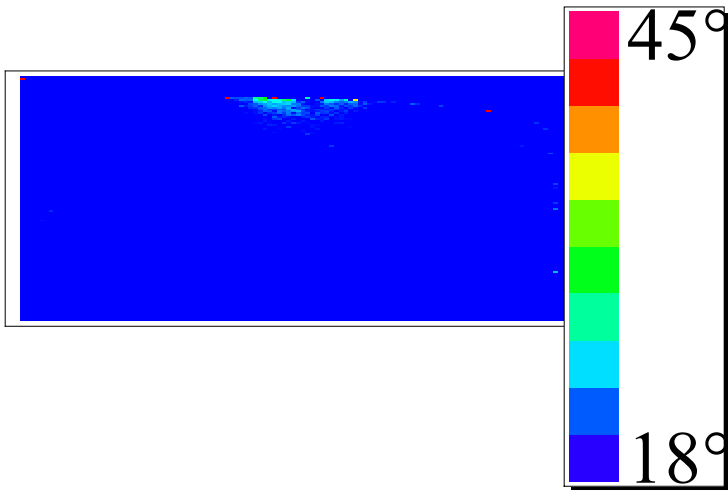


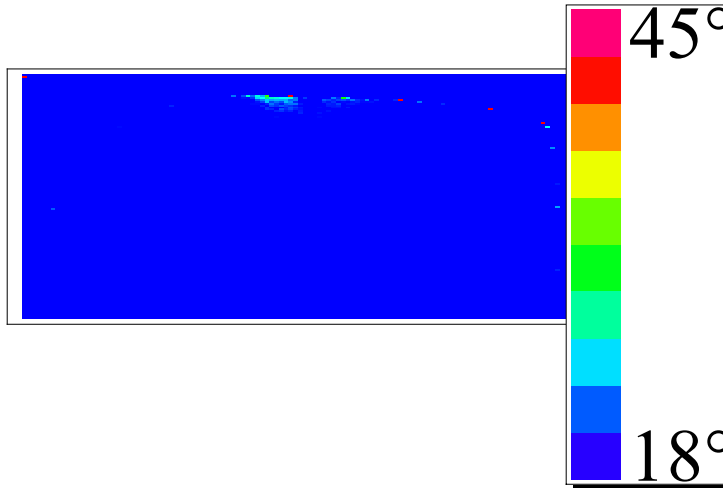












In[222]:=

```
T = Table[ InitialT + datafinal[[i]],
  {i, 1, cycle}];
```

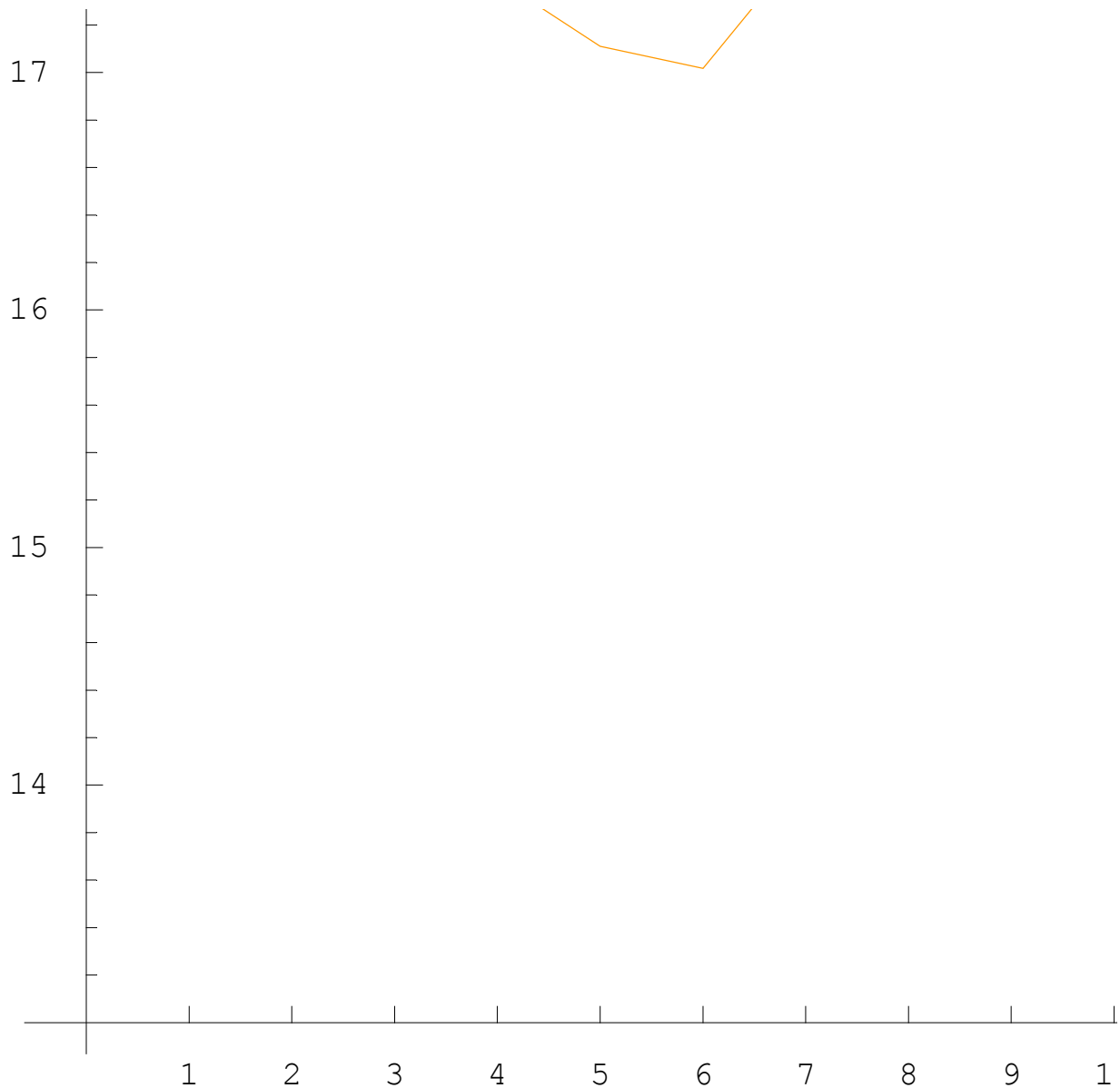
In[223]:=

```
PL[data_] :=
  ListPlot[data, PlotStyle -> {PointSize[.02], Hue[.1]}, PlotJoined -> True,
    Ticks -> {Range[34], Automatic}, AxesLabel -> {"Phases", "T"},
    PlotLabel -> "TYPE HERE", TextStyle -> {FontSize -> 14}];
```

In[224]:=

```
PL[T]
```





Out[224]= - Graphics -

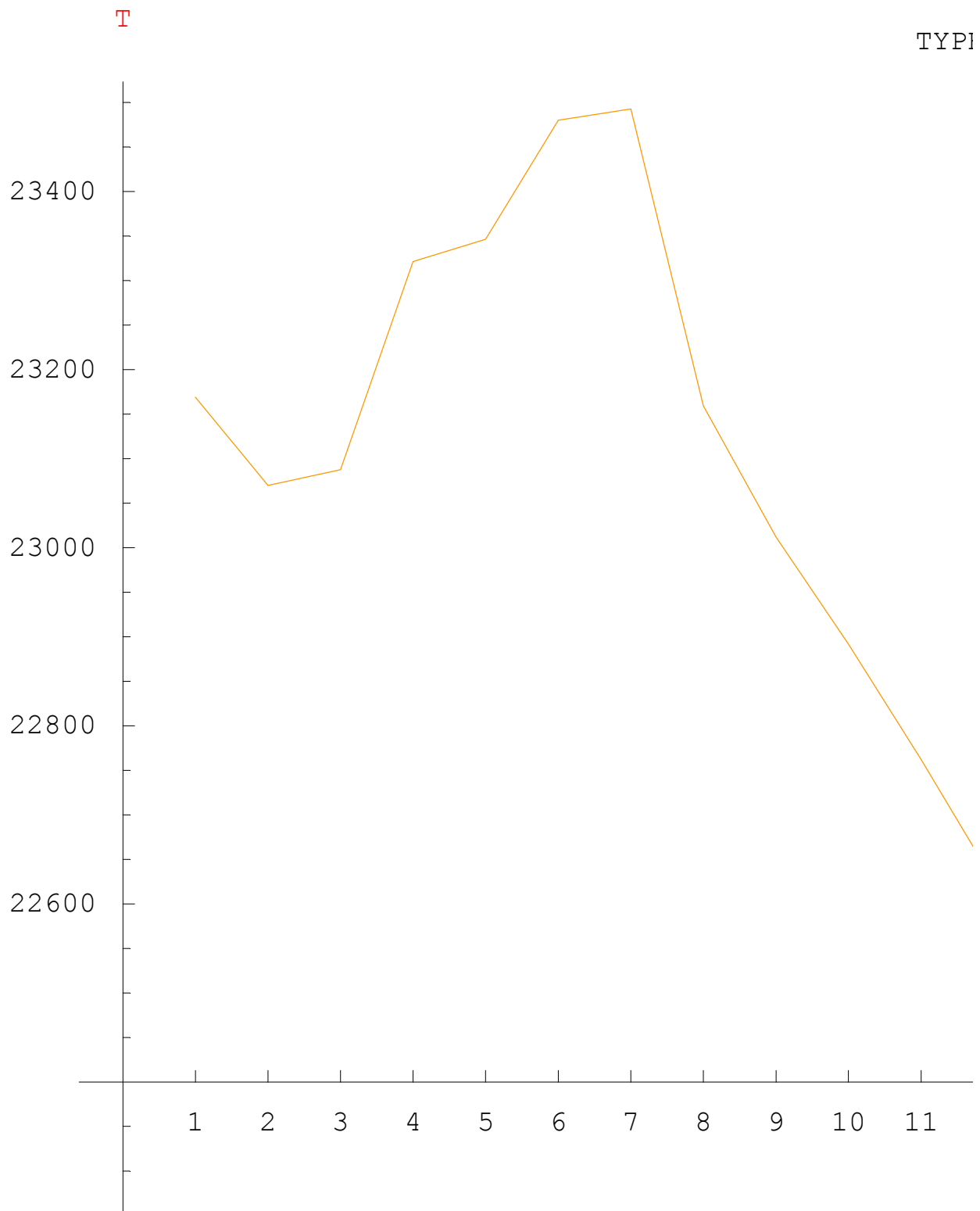
```
In[225]:= (*the folowing function export datafinal to the excel format .xls;  
note the \ / signs are very picky*)
```

```
In[226]:= Export["C:\Users\Kelvin\Desktop\data1.xls", T];  
mag = Table[d2mow[[i]][[slice]], {i, 1, cycle}];  
Export::nodir : Directory C:\Users\Kelvin\Desktop\ does not exist. More..
```

```
In[228]:= box5 = func[mag, cycle, xo, xt, yo, yt];
```

```
In[229]:= box6 = AVERAGE [ box5 ] ;
```

```
In[230]:= PL[box6]
```



---

Out[230]= - Graphics -